Constraints from GPS measurements on the dynamics of the zone of convergence between Arabia and Eurasia

R. J. Walters[1,2], P. C. England[3], and G. A. Houseman[1]

R. J. Walters, Department of Earth Sciences, Durham University, Elvet Hill, Durham DH1 3LE, UK.

[1]COMET, Department of Earth Sciences,

Durham University, Elvet Hill, Durham

DH1 3LE, UK.

[2]COMET, School of Earth and

Environment, University of Leeds, Leeds

LS2 9JT, UK.

[3]Department of Earth Sciences,

University of Oxford, South Parks Road,

Oxford OX1 3AN, UK.

Abstract.   We investigate the dynamics of deformation in the zone of convergence between the Arabian and Eurasian plates using a physical model that treats the lithosphere as a thin fluid sheet deforming in response to lateral variations in gravitational potential energy (GPE). This model has two free material parameters, the power-law exponent, n, of the vertically-averaged rheology of the lithosphere, and the Argand number, Ar, which expresses the relative importance of GPE and stresses required to deform the lithosphere. With boundary conditions described by three free parameters, the model fits the observed deformation, as measured by 367 GPS velocities, with a root-mean-square residual of $<$ 2.4 mm/yr. We find negligible improvement when variations in material properties are introduced that represent increases or decreases in the lithospheric strength of the Central Iranian and Turkish-Iranian Plateaux and the Zagros Mountains. Effective viscosity of the lithosphere ranges from 5×10^{22} Pa s at 10 nanostrain/yr to 10^{22} Pa s at 100 nanostrain/yr. As well as matching the decadal-timescale, predominantly interseismic, strain rates determined from GPS, the computed distribution of strain rates is also consistent with the distribution and types of earthquake focal mechanism. Significant historical earthquake activity is seen in regions with strain rates lower than 20 nanostrain/yr, implying that it is prudent to base assessments of seismic hazard on regional strain rates.

Keypoints:

- A physical model that treats the lithosphere as a homogeneous fluid sheet accounts for 95% of the variance in GPS velocities.

- Lateral variations in physical properties of lithosphere are not required in order to explain the large-scale deformation.

- Distributions of faulting and seismic hazard are determined by lateral variations in gravitational potential energy of the lithosphere.

1. Introduction

In the longitude range 40–62°E, oblique convergence between the Arabian and Eurasian plates at 20-30 mm/yr [*Reilinger et al.*, 2006] is accommodated within a region approximately 2000 km long (NW-SE) and between 500 and 1000 km wide which covers Iran, Azerbaijan, and parts of Turkey and Armenia [*e.g. Engdahl et al.*, 2006; *Hatzfeld and Molnar*, 2010; *Jackson and McKenzie*, 1988; *Tatar et al.*, 2004; *Walker and Jackson*, 2004, and Figure 1]. The surface manifestation of this deformation is a combination of reverse and strike-slip faulting, seen both in the geomorphic expression of the late-Quaternary faulting and in the focal mechanisms of earthquakes [*e.g. Baker et al.*, 1993; *Berberian and Yeats*, 1999; *Copley and Jackson*, 2006; *Engdahl et al.*, 2006; *Fattahi et al.*, 2006; *Foroutan et al.*, 2012; *Hollingsworth et al.*, 2006, 2010; *Jackson and McKenzie*, 1988; *Jackson et al.*, 2002; *Javidfakhr et al.*, 2011; *Le Dortz et al.*, 2009, 2011; *McKenzie*, 1972; *Meyer and Le Dortz*, 2007; *Meyer et al.*, 2006; *Nazari et al.*, 2009; *Shabanian et al.*, 2009, 2010; *Regard et al.*, 2005; *Talebian and Jackson*, 2002; *Walker et al.*, 2009; *Walker and Jackson*, 2004; *Walker et al.*, 2010, and see Figure 1]. West of ∼57°E this convergence is accommodated within the continental lithosphere of Eurasia by a combination of reverse and right-lateral strike-slip faulting in the Zagros, in the mountain ranges of the Alborz and Caucasus, and by convergence across the Apsheron-Balkhan Sill [*e.g. Jackson et al.*, 2002]. East of 57°E, approximately three-quarters of the convergence is accommodated by the Makran subduction zone [*Vernant et al.*, 2004], with the remaining shortening taken up within the Kopeh Dagh and other mountain ranges in NE Iran. Right-lateral shear

between central Iran and Afghanistan is accommodated by N-S trending strike-slip faults in eastern Iran.

Seismicity and active faulting are concentrated in the Zagros, Alborz, Talysh and Kopeh Dagh mountain ranges, and in eastern Iran (Figure 1); these zones separate the relatively aseismic regions of the Central Iranian Plateau, the south Caspian Sea and the Lut desert, which have been interpreted as quasi-rigid blocks whose relative motions are taken up by deformation in the surrounding mountain ranges [*e.g. Jackson and McKenzie*, 1988]. While subsets of the GPS velocities in Iran have been used to describe the kinematics by the relative motions of rigid blocks [*e.g. Reilinger et al.*, 2006; *Walpersdorf et al.*, 2014], the velocity measurements are too sparse except in a few small areas (Figure 2b), to permit more than $\sim 5-10$ velocity measurements per block, so it is hard to test such models rigorously.

The occurrence of M$\gtrsim$ 6 earthquakes within central Iran suggests that the plateau may not be rigid [*Jackson and McKenzie*, 1984], a suggestion that is supported by field evidence of faults that have produced earthquakes in Holocene time [*e.g. Foroutan et al.*, 2012; *Le Dortz et al.*, 2009, 2011; *Meyer and Le Dortz*, 2007; *Meyer et al.*, 2006; *Nazari et al.*, 2009] and by recent GPS studies that show measurable strain rates in the region [*e.g. Masson et al.*, 2005, 2007, 2014]. An alternative interpretation of the low rates of strain in central Iran is that they represent a state of low deviatoric stress in which the compressional stresses applied to the region are balanced by its higher gravitational potential energy [*e.g. Hatzfeld and Molnar*, 2010].

We use the GPS determinations of surface velocities in Iran and neighboring regions to constrain a set of numerical experiments that investigate the extent to which lateral

variations in gravitational potential energy and in physical properties of the lithosphere control the distribution of faulting, seismicity and seismic hazard in Iran.

2. Physical Model

The physical model treats the continental lithosphere as a sheet of material whose deformation is determined by the vertical averages of its mechanical properties and of the forces acting upon it – the thin sheet approximation, in which horizontal gradients of the deviatoric stress associated with deformation of the lithosphere are balanced by gradients of the gravitational potential energy per unit area of lithosphere (GPE), *Bird and Piper* [1980]; *England and McKenzie* [1983]; *Houseman and England* [1986]. Here we outline the principal features of the model; details and means of solution are to be found in Appendix A2 and in *England et al.* [2016].

2.1. Gravitational Potential Energy

It has often been suggested that deformation of the continental lithosphere represents a balance between lateral variations in gravitational potential energy and the stresses required to deform the lithosphere [*e.g. Dalmayrac and Molnar*, 1981; *England and McKenzie*, 1982; *England and Molnar*, 1997; *England and Houseman*, 1989; *Frank*, 1972; *Houseman and England*, 1986; *Jones et al.*, 1996; *McKenzie*, 1970, 1972; *Molnar*, 1988; *Molnar et al.*, 1993; *Molnar and Lyon-Caen*, 1988; *Molnar and Tapponnier*, 1978]. The gravitational potential energy per unit area (GPE) of a column of lithosphere, Γ, is

$$\Gamma = g \int_0^{L+h} \rho(z)\, z\, \mathrm{dz}, \tag{1}$$

where h is surface height, z is positive upwards and the level $z = 0$ is taken to be at a depth L, the nominal lithospheric thickness, below the geoid. If the column is in a state

of local isostatic balance, the GPE is proportional to the depth-averaged vertical stress

$$\sigma_{zz} = -g \int_z^{L+h} \rho(z)\,\mathrm{d}z \tag{2}$$

$$\overline{\sigma}_{zz} = \frac{-1}{(L+h)} \int_0^{L+h} \int_z^{L+h} \rho(z')\,\mathrm{d}z'\,\mathrm{d}z = \frac{-\Gamma}{(L+h)} \tag{3}$$

[*e.g. Parsons and Richter*, 1980].

We calculate the GPE in two ways, in each case assuming that all the columns of lithosphere are in isostatic balance with a reference column of lithosphere, with GPE Γ_0, crustal thickness S_0, and surface elevation h_0 (Table 3). One method assumes Airy isostatic balance, using the distribution of surface height shown in Figure 1. We define a reference column of lithosphere, with crustal thickness S_0, and surface elevation h_0 (Table 3). Surface height is related to crustal thickness, S, under the assumption of Airy isostatic balance

$$S - S_0 = \frac{\rho_m}{\rho_m - \rho_c}(h - h_0), \tag{4}$$

where ρ_c and ρ_m are the average densities of crust and mantle. For uniform crust overlying uniform mantle, the difference in GPE between the reference column, of GPE Γ_0, and a column with crust of thickness S is

$$\Delta\Gamma = \Gamma - \Gamma_0 = g\rho_c(h - h_0)\left(S_0 + \frac{\rho_m(h - h_0)}{2(\rho_m - \rho_c)}\right) \tag{5}$$

where g is the acceleration due to gravity[*Haxby and Turcotte*, 1978].

The presence of widespread volcanism across the Turkish-Iranian Plateau suggests, however, that there may be significant lateral variation in the density of the mantle beneath the region, and evidence from seismic receiver functions and surface wave tomography also indicate that the elevation of the plateau is partly supported by relatively-low-density lithospheric mantle [*Al-Lazki et al.*, 2003, 2004, 2014; *Alinaghi et al.*, 2007; *Amini et al.*,

2012; *Innocenti et al.*, 1976; *Kaviani et al.*, 2007; *Maggi and Priestley*, 2005; *Mutlu and Karabulut*, 2011; *Şengör et al.*, 2003; *Zor et al.*, 2003]. We therefore also estimate differences in GPE from differences in geoid height ΔN

$$
\begin{aligned}
\Delta N &= -\frac{2\pi G}{g} \int_0^{L+h} z \Delta\rho(z)\mathrm{d}z \\
&= \frac{2\pi G}{g^2} \Delta\Gamma
\end{aligned}
\tag{6}
$$

[*Haxby and Turcotte*, 1978, and see Eq. (1)], where G is the gravitational constant and $\Delta\rho$ is difference between the density and density at the same level in the reference column.

Figure 3a shows the GPE estimated from the SRTM 3-arc-second topography [*Farr et al.*, 2007], smoothed with a Gaussian filter of width 100 km. Figure 3b shows GPE calculated from the EGM08 geoid model [*Pavlis et al.*, 2012]. To remove long-wavelength contributions to the geoid, the model is truncated below degree and order 8, and a tapered filter is applied between degrees and orders 8 and 12; the taper, which was chosen so that the geoid height along the coast of Iran remains approximately constant, is similar to that used by *Chase et al.* [2002] to calculate the lithospheric contribution to the geoid. The main differences between the two estimates of GPE are in the Turkish-Iranian Plateau and at the south-east end of the Central Iranian plateau, where the GPE estimated from geoid variations is higher than that estimated from Airy isostasy, and in the Zagros, where the GPE estimated from geoid variations is lower than that from isostasy.

2.2. Mechanical properties

The mechanical properties of the sheet are described by a power-law relation between the vertically averaged components of deviatoric stress and strain rate:

$$
\overline{\tau}_{ij} = B\dot{E}^{\left(\frac{1}{n}-1\right)}\dot{\varepsilon}_{ij}
\tag{7}
$$

where $\dot{\varepsilon}_{ij}$ is the ij^{th} component of the strain-rate tensor, assumed constant with depth through the sheet, $\overline{\tau}_{ij}$ is the ij^{th} component of the deviatoric stress tensor, with the over-bar denoting averages over the thickness, L, of the lithosphere and

$$\dot{E} = (\dot{\varepsilon}_{kl}\dot{\varepsilon}_{kl})^{\frac{1}{2}} \tag{8}$$

is the second invariant of the strain-rate tensor, with the convention of summation over repeated indices. The fluid is assumed to be incompressible ($\dot{\varepsilon}_{kk} = 0$).

The viscosity coefficient, B, and the power-law exponent in the rheology, n, define the physical properties of the lithosphere. The quantity

$$\eta_{\text{eff}} = \frac{1}{2}B\dot{E}^{\left(\frac{1}{n}-1\right)} = \frac{1}{2}B^n\overline{T}^{(1-n)}, \tag{9}$$

where $\overline{T}$ is the second invariant of the vertically-averaged deviatoric stress tensor, $(\overline{\tau}_{kl}\overline{\tau}_{kl})^{\frac{1}{2}}$, is commonly referred to as the effective viscosity, by analogy with the viscosity of a Newtonian fluid in the case that $n = 1$. Note that for $n \neq 1$ the effective viscosity depends on the deviatoric stress, or equivalently upon strain rate, so that lithosphere of spatially invariant viscosity coefficient, B, will in general exhibit lateral variation in its effective viscosity.

The relative importances of deviatoric stresses required to deform the lithosphere and GPE are expressed by the Argand number

$$Ar = \frac{g\rho_c(1 - \rho_c/\rho_m)L}{B(U_0/L)^{1/n}} \tag{10}$$

[*England and M$^{\text{c}}$Kenzie*, 1982], where g is the acceleration due to gravity, ρ_c and ρ_m are the average densities of crust and mantle respectively, and U_0 is a scale velocity. In what follows, the results of dimensionless calculations are expressed in dimensional terms using the values of parameters given in Table 3. The spatial variations of strain rate and velocity

depend, however, only upon the value of Ar, not upon the individual quantities within it (see Appendix A2).

2.3. Region of interest, and boundary conditions

We divide the border to the calculation domain into seven sections whose lengths and locations are dictated by their geological settings (Figure 3). The choice of a small number of long boundary segments is justified by a fundamental aspect of the governing equations. When, as is the case in this study, the boundary conditions are of normal velocity or traction they influence strain rates over a distance from that boundary that is $\sim D/\sqrt{n}$, where n is the exponent in the power-law rheology (equation (7)) and D is the length of the boundary [*England et al.*, 1985]. It follows that any variation in boundary condition over a scale that is small compared with the length scale of the calculation domain has only a local influence, and does not significantly affect the distribution of stresses and velocities in the region as a whole.

We use a reference frame fixed to stable Eurasia. Where the calculation domain is directly in contact with a plate or (as in the case of the South Caspian) a smaller block that appears to be rigid, we assign a velocity boundary condition (segments EU, AR, and SC, Figure 3). The northern boundary is placed along the sharp topographic contrasts between Iran and the Caucasus, the Caspian Sea, and Eurasia. We treat this boundary (segment EU in the north of Figure 3) as lying within stable Eurasia and therefore set the velocity on this boundary to zero. We assign zero velocity to the eastern boundary, which follows approximately the border between Iran and Afghanistan (segment EU in the east of Figure 3) because estimates of seismic moment release and GPS measurements show that Afghanistan is moving slowly with respect to Eurasia [*Ambraseys and Bilham*,

2003; *Masson et al.*, 2005]. Apart from the subduction zone of the Makran, the southern boundary of our calculation domain follows the Iranian coast and the marked step in topography between Iraq and the Turkish-Iranian plateau (segment AR, Figure 3). These sharp topographic features approximate the boundary between the Arabian plate and deforming Iran; we fix the velocity on this segment using an angular velocity estimated from GPS sites within Arabia that lie close to the boundary. This angular velocity has a pole at 18.1°E, 26.5°N, and a rotation rate of 0.38°/Myr, which differs slightly from the Arabia-Eurasia angular velocity of *Reilinger et al.* [2006] because of internal deformation of Arabia near this boundary.

The southern Caspian Sea moves relative to Eurasia [*Jackson and McKenzie*, 1984; *Jackson et al.*, 2002; *Copley and Jackson*, 2006] at approximately 11 mm/yr at an azimuth of 335° [*Copley and Jackson*, 2006]. We apply that velocity condition to the boundary segment corresponding to the southeast and south coasts of the Caspian Sea (segment SC in Figure 3); the fits to the observed velocities are almost identical if we use the slightly different definition of the South Caspian motion of *Djamour et al.* [2010]. The relative velocities across three boundaries (Segments M, SWC, and T, Figure 2) are poorly constrained. The section of the southern boundary east of 57.2°E (segment M, Figure 3) lies to the north of the Makran subduction zone, which accommodates much of the Arabia-Eurasia convergence at this longitude; the choice of a velocity condition for this boundary is, therefore, uncertain. A similar uncertainty arises at the border of the southwest Caspian Sea (Segment SWC in Figure 3); the occurrence of reverse-faulting earthquakes on shallowly dipping planes suggests that the South Caspian is being thrust beneath the bordering continental lithosphere in this region [*Jackson and McKenzie*, 1984; *Jackson*

et al., 2002; *Copley and Jackson*, 2006]. The third segment (T, Figure 3) represents the transition between predominantly contractional deformation in Iran and neighboring regions and the zone of horizontal simple shear and extension in central Anatolia and the Aegean, which is the subject of a separate study [*England et al.*, 2016]. At these boundaries to the calculation domain we apply normal forces per unit length, respectively Γ_M, Γ_C, and Γ_T, and allow these forces to be free parameters in the search described in Section 4.

2.4. Observations of crustal velocity

We constrain our analysis with crustal velocities determined using the Global Positioning System (GPS). Geodetic measurements of the deformation of the lithosphere are taken at the top of the upper crust, which in general deforms elastically. We take the view that the strain of this thin elastic layer follows closely the ductile strain of the layer beneath [*e.g. Bird and Piper*, 1980; *Bourne et al.*, 1998; *Houseman and England*, 1986]. Furthermore, except during the post-seismic intervals of nearby earthquakes, the ductile strain rate may be considered time-invariant on the time scale of geodetic observation. This view contrasts with interpretations of velocity fields that treat the lithosphere as an elastic medium whose surface deformation is controlled by the slip of dislocations buried within it [*e.g. Hammond et al.*, 2011; *Meade et al.*, 2002; *Meade and Hager*, 2005; *Reilinger et al.*, 2006; *Wallace et al.*, 2007].

Kreemer et al. [2014] combined published measurements of *Aktuğ et al.* [2013a, b]; *Djamour et al.* [2010, 2011]; *Hessami et al.* [2006]; *Kadirov et al.* [2012]; *Karakhanyan et al.* [2013]; *Mousavi et al.* [2013]; *Peyret et al.* [2009]; *Reilinger and McClusky* [2011]; *Reilinger et al.* [2006]; *Tatar et al.* [2012]; *Tavakoli et al.* [2008]; *Walpersdorf et al.* [2006, 2014]

and their own processing of continuous GPS sites. They report 630 determinations of velocity from within our area of interest, but 195 of these are duplicated between different studies. We removed all duplicates, retaining only the most recently published velocity for each site, presuming those velocities to be based on the greatest number of reliable occupations for each site, and on the most modern processing strategies. We also eliminate a further 68 sites having a formal error greater than 2 mm/yr in their velocity, leaving 367 measurements of horizontal velocity within the region shown in Figure 2a.

Interpretation of the dynamics of the deformation depend on knowledge of strain rates, which we calculate from the GPS observations using the method of *Shen et al.* [2015] (Section A1). The principal horizontal axes of strain rate are displayed in Figure 2b on an equidimensional surface grid with points separated by angular distance of 1 degree.

3. Preliminary Analysis

We first ask whether the observed distribution of velocities shows any influence from lateral variations in GPE, following an analysis suggested by *D'Agostino et al.* [2014]; *Dalmayrac and Molnar* [1981], and *England and Molnar* [2015]. In the central part of the orogen, between about 50° and 54°E, the velocities and principal horizontal contractional strain rate axes are both aligned approximately north-south (Figure 2), which allows us to use an approximate analytical solution to the thin-sheet equations (Eqs. (A1)). We analyse the velocities within 200 km of profile X-X' in Figure 2. Neglecting the component of velocity in the direction perpendicular to the profile, and integrating the thin-sheet equation in the direction parallel to the profile yields an expression that relates

the integral of GPE along the profile to the velocity, u_x, in the same direction

$$u_x = U_1 + \frac{(U_2 - U_1)\,x}{W} + \frac{1}{4\eta_{\text{eff}}L}\left[\int_0^x \Delta\Gamma(x')\mathrm{d}x' - \frac{x}{W}\int_0^W \Delta\Gamma(x')\mathrm{d}x'\right], \qquad (11)$$

where W is the length of the profile, U_1 and U_2 are the values of velocity at the south $(x = 0)$ and north $(x = W)$ ends of the profile, η_{eff} is the effective viscosity of the lithosphere, assumed constant along the profile, and $\Delta\Gamma$ is the difference between the GPE of the lithosphere at a point on the profile and that at $x = 0$ (Appendix A3).

Figures 4a and b show the variation of topography, and of integrated GPE calculated from topography using Eq. (5), along the profile X_1–X_2 of Figure 2. Figure 4c shows the variation of u_x measured at GPS sites within 200 km of the profile and the linear least-squares fit to these velocities, which has an RMS misfit of 1.5 mm/yr. The values of the parameters to this fit are: $U_1, U_2 = 23$ and 7 mm/yr and $4\eta_{\text{eff}}L = 2 \times 10^{27}$ N m^{-1} s which, for $L \sim 100$ km, is equivalent to an effective viscosity for the lithosphere of $\sim 5 \times 10^{21}$ Pa s. The principal features of the velocity variation are explained by the variation in GPE along the profile. Contractional strain (northward decrease of northerly velocity) occurs at the south of the profile where the topography (and GPE: Eq. 5) is low; the contractional strain rate drops close to zero over the Central Iranian Plateau ($\sim$300-700 km on the profile) then increases again to the north ($\sim$800-1100 km on the profile), as the surface height decreases. This analysis suggests that the lithosphere of the region deforms in response to lateral variations in its gravitational potential energy. The compressional stresses at the southern border of Iran are transmitted to northern Iran via the higher lithostatic stresses beneath the plateau, in a fashion analogous to that described by *Molnar and Tapponnier* [1978] for Tibet [see also *Hatzfeld and Molnar*, 2010].

4. Estimation of physical parameters

Turning now to the two-dimensional problem constrained by the boundary conditions and GPE distribution indicated in Figure 3, we seek values for the five parameters that will allow an adequate fit to the observed GPS velocity field. Three parameters are the forces per unit length Γ_M, Γ_C, and Γ_T applied at the boundary segments corresponding to the Makran, the South Caspian, and eastern Turkey. The other two define the physical properties of the lithosphere: the exponent n in the power-law rheology (Eq. (7)) and the Argand number, Ar (Eq. (10)). We assume for now that the rheological parameters n and B are spatially invariant.

4.1. Parameter search

The governing equations are solved subject to the boundary conditions described in Section 2.3, and with the distribution of GPE derived both from topography and from the EGM08 geoid model (Section 2.1), using a finite-element approximation to the equations for deformation on the surface of a sphere (see Appendix A2). The finite-element mesh contains 5,400 nodal points, 367 of which are placed at the locations of the GPS sites. The mean spacing between nodal points is approximately 20 km, significantly smaller than the mean spacing between GPS sites (Figure 2a).

For each combination of parameters, we quantify the misfit between our calculated velocities, $\mathbf{u}_i^{C}$, and the GPS velocities, $\mathbf{u_i^{GPS}}$, by the weighted root-mean-square misfit, M:

$$ M = \left[\frac{1}{N} \frac{\sum\limits_{i=1}^{N} \left| \mathbf{u}_i^{GPS} - \mathbf{u}_i^{C} \right|^2 V_i}{\sum\limits_{i=1}^{N} V_i} \right]^{\frac{1}{2}} \tag{12} $$

where V_i are the Voronoi areas of the N GPS sites (Section A1). We use weighted RMS misfits in the parameter search in order to avoid biasing our fit towards regions with

highest density of GPS observations but, in discussing the quality of the fits, we quote the RMS misfit to all the observations, weighted equally:

$$\left[\frac{1}{N}\sum_{i=1}^{N}\left|\mathbf{u}_i^{\text{GPS}}-\mathbf{u}_i^{\text{C}}\right|^2\right]^{\frac{1}{2}} \tag{13}$$

We checked the resolution of the calculations using meshes of 10,000 points and found that neither measure of misfit differed by more than ~1% between the two meshes.

The Makran boundary segment is about 400 km long and lies further than this distance from all but about 10 GPS observations (Figure 2). By the argument of Section 2.3, the condition applied at this boundary has little influence on the rest of the solution.; we therefore estimate the parameter Γ_M independently of the others. For $n = 1, 3, 5$, and 9, and with GPE estimated from the EGM08 geoid (Section 2.1 and Figure 3b), we varied Ar and Γ_M, finding the value of Γ_M that produces the minimum misfits to velocities. These values were -0.625 TN m^{-1}, $(n = 1)$; -3.0 TN m^{-1}, $(n = 3)$; -2.75 TN m^{-1}, $(n = 5)$ and -4.0 TN m^{-1}, $(n = 9)$. Each of these corresponds to a compressional force per unit length. For subsequent calculations with $n = 3, 5$ and 9 we fix Γ_M to -3.0 TN m^{-1}, the best-fitting value for $n = 3$, rather than imposing a different boundary condition for each value of n. For $n = 5$ and 9 this value fits the observations almost as well (difference of less than 0.01 mm/yr in M) as the best-fitting value. For $n = 1$ we use $\Gamma_M = -0.6$ TN m^{-1}.

We then systematically searched the four-parameter space (n, Ar, Γ_T, and Γ_C), finding the values of the parameters that best fit the observations with GPE estimated both from topography and from the EGM08 geoid (Section 2.1 and Figure 3). For $n = 1, 3, 5$, and 9, we varied Ar from 0 to 10 in steps of 0.25, and from 10 to 30 in steps of 0.5, and varied Γ_T in steps of 0.125 TN m^{-1} from -6 to 1 TN m^{-1} and Γ_C from -4 to 4 TN m^{-1}. The best-fitting values are listed, with their associated misfits, in Table 1 and shown in Figure 5. The best-

fitting calculations with GPE calculated from topography have RMS misfits (Eq. (13))
in the range 2.8 to 3.2 mm/yr. The calculations using GPE derived from the geoid fit
the data better (Figure 5b-f and Table 1), with RMS misfits between 2.3 and 2.4 mm/yr.
For these calculations, the range of the best-fitting force per unit length on the boundary
segment corresponding to eastern Turkey, Γ_T, is -1.75 to -2.75 TN m^{-1}. The GPE of
the region immediately inside the boundary is between 2 and 2.5 TN m^{-1} (Figure 3b),
consistent with the middle of the range of best-fitting Γ_T. The best-fitting force per unit
length on the boundary segment corresponding to the south-west coast of the Caspian,
Γ_C, differs from zero, for $n > 1$, by less than 0.5 TN m^{-1}.

4.2. Lateral heterogeneity in viscosity coefficient

The solutions presented so far have constant material properties. The viscosity coeffi-
cient, B, is spatially invariant and the effective viscosity of the lithosphere varies solely
in response to variations in strain rate (Eq. (9)). It is reasonable, however, to investigate
whether there may be large-scale variations in B. For example, it has been suggested that
the Central Iranian Plateau is a quasi-rigid micro-plate, or at least a region of intrinsi-
cally greater strength than its surroundings [*e.g. Jackson and McKenzie*, 1988; *Sobouti
and Arkani-Hamed*, 1996]. In contrast seismic wave speeds in the upper mantle are lower
beneath the plateaux of central and north-western Iran than beneath surrounding re-
gions, suggesting that these regions are underlain by hot, weak uppermost mantle and
may therefore be intrinsically weaker than their surroundings. Wave speeds below the
Zagros Mountains are higher, suggesting that this region may have stronger upper mantle
[*e.g. Al-Lazki et al.*, 2003, 2004, 2014; *Alinaghi et al.*, 2007; *Amini et al.*, 2012; *Kaviani
et al.*, 2007; *Maggi and Priestley*, 2005; *Mutlu and Karabulut*, 2011; *Priestley et al.*, 2012].

We investigate this issue by defining three regions in which we allow the value of B to be a multiple, B', of the value for the rest of the domain of calculation. The first of these regions corresponds to the region of Holocene volcanic activity in the north-western end of the Turkish-Iranian Plateau (TIP in Figure 6a); the second corresponds to the Central Iranian Plateau (CIP in Figure 6a) and the third to the Zagros Mountains (ZAG in Figure 6a). We first allow B' to vary separately in each region between 0.1 and 10, holding $n = 3$. Γ_T and Γ_C were fixed to their best-fitting values for the calculations with spatially invariant material properties (Table 1). The variations of misfit with B' and Ar are shown in Figure 6b (Turkish-Iranian Plateau), Figure 6c (Central Iranian Plateau), and Figure 6d (Zagros). The best-fitting solutions are $B'_{TIP} = 1.1$ with $M = 2.7$ mm/yr, $B'_{CIP} = 0.8$ with $M = 2.7$ mm/yr, $B'_{ZAG} = 0.85$ with $M = 2.6$ mm/yr (Table 2). The reduction in misfit, in comparison with the best-fitting solutions for the homogeneous sheet ($M = 2.7$ mm/yr, Table 1), is negligible.

We next allowed the value of B' to vary in all three regions simultaneously, finding the best-fitting combination of Ar, B'_{TIP}, B'_{CIP}, and B'_{ZAG} using the down-hill simplex minimisation of Nelder and Mead [*Press et al.*, 1992]. The best-fitting solution gave $B'_{TIP} = 1.2$, $B'_{CIP} = 1.0$, $B'_{ZAG} = 0.83$ with $M=2.6$ mm/yr, and an RMS misfit of 2.2 mm/yr (Table 2). To check whether this procedure had settled on a local minimum, we calculated M for 100,000 random combinations of the parameters within the ranges shown in Figure 7, finding no combination of parameters that produced a lower misfit than that obtained in the inversion. Of these 100,00 solutions, those in which B' within the Turkish-Iranian plateau lies outside the range 0.7 to 1.8 fit the data worse than calculations with a homogeneous lithosphere; the equivalent range of B' for the Zagros is

0.7 to 1.0. The lower bound for B' in the Central Iranian plateau is 0.6 but an arbitrarily high B' for this region is permitted by the observations (Figure 7). There appears to be no trade-off between the parameters, and the ranges of acceptable values are very similar to those obtained when the B's are varied separately (Figure 6).

5. Discussion

5.1. Comparison with observed velocities and strain rates

The RMS magnitude of the velocities measured with GPS in the convergence zone between Arabia and Eurasia (Figure 2) is 11.6 mm/yr; the best-fitting calculation for the homogeneous sheet with GPE calculated from the geoid fits the observations with an RMS misfit of ≤2.4 mm/yr, a reduction in the original variance of 95% (Table 1). Observed velocities are compared with those from the homogeneous sheet with $n = 3$ in Figure 8a,b; of the 367 GPS velocities, 256 are fit to within 3 mm/yr. When B' is allowed to vary simultaneously in all three regions, the best-fitting calculation fits 267 GPS velocities to within 3 mm/yr (Figure 8c). For each calculation a set of observations in the Zagros, marked by black circles in Figures 8b and c, are misfit by ~5 mm/yr whereas nearby sites are fit to better than 3 mm/yr. These sites are all from the study of *Hessami et al.* [2006], who report that their limited number of receivers did not allow the complete network to be measured in one session; it is possible that these larger misfits result from a problem with reference frames in that study. A similar consideration may apply to parts of the south-east Caspian coast, and to the region around 45°E, 39°N, where a few sites have large misfits, among larger groups with small misfits.

There are clusters of misfitting vectors in the Zagros-Makran transition zone, near the eastern and western coasts of the South Caspian, and at the boundary with Turkey at

about 40°E, 40°N. The misfits in Zagros-Makran transition zone are confined to a region about 200 km on a side, in which the boundary conditions are probably more complicated than those we use here, and we do not consider these misfits further. The areas of misfit around the South Caspian and at the boundary with Turkey also have length scales of a couple of hundred kilometres, and lie close to the boundaries of our calculation domain. By the arguments of Section 2.3, these misfits could be reduced by adjustments to the boundary conditions in their immediate neighborhood without influencing conclusions about the large-scale deformation. For example, the observed velocities near the southwest Caspian coast (segment SWC, Figure 3) have a larger northerly component than do the calculated velocities; these misfits would be reduced by a corresponding increase in the northerly component of velocity on this section of the boundary. *England et al.* [2016] demonstrated the viability of reducing residuals by local adjustments to the boundary conditions, and the insensitivity of the overall solution to such adjustments, but we do not repeat that exercise here.

Figure 9a shows the horizontal principal axes of strain rate derived from the GPS observations, at the 155 geographical locations of the grid shown in Figure 2b, superimposed on the second invariant of the corresponding strain-rate tensor. Figures 9b,d,e compare those observations with the results of the best-fitting calculations for the homogeneous sheet (Figure 8a,b). Observed strain rates range from 5 to over ~ 60 nanostrain per year; at 141 out of the 155 locations the calculated and observed rates agree to within a factor of two (Figure 9d). In 123 out of the 155 locations the calculated and observed azimuths agree to within 20° (Figure 9c). Figures 9c,f,g make the same comparisons for the calculations with lateral variations in strength (Section 4.2 and Figure 8c). As with

the fit to velocities, the influence of permitting lateral variations in B is negligible: the number of locations in which the calculated and observed rates agree to within a factor of two increases to 143, while the number of locations in which the calculated and observed azimuths agree to within 20° decreases to 121.

The RMS misfit of 2.4 mm/yr between calculated and observed velocities suggests that the thin-sheet model accounts for the principal features of the deformation of Iran, as measured by the current geodetic data. The remaining misfits between observation and model may be attributed partly to data inconsistencies (see, for example, discussion of misfits at the beginning of this subsection) and partly to local deviations from the continuous behaviour expected of a viscous lithosphere, due to shallow tectonic movements, to non-tectonic movements, or to monument instability. The agreement between observed and calculated strain rate fields, at the scale of 100 km (Figure 9), allows us to investigate the implications of this model for the rheology of the lithosphere, for active faulting, and for seismic hazard.

5.2. Rheology of the lithosphere

The viscosity coefficient for the lithosphere obtained from the calculations with spatially invariant material properties and $n = 3$ is $B = 2.2 \times 10^{12}$ Pa s$^{1/3}$, which yields effective viscosities in the range $5 \times 10^{22} - 10^{22}$ Pa s at strain rates of 10 to 100 nanostrain per year (Figure 10), consistent with the preliminary analysis (Section 3). The range is similar for $n = 5$ and 9. This range of effective viscosity is comparable with estimates made for other regions of active continental deformation. Using the approach employed here, *England et al.* [2016] estimated the viscosity coefficient, B, of the lithosphere in Anatolia to be 6.0×10^{11} Pa s$^{1/3}$ for a homogeneous sheet with $n = 3$, which corresponds to

effective viscosity of the lithosphere in the range 10^{22} to 3×10^{21} Pa s at strain rates of 10 to 100 nanostrain per year. Allowing the material properties of the lithosphere to vary spatially, *Özeren and Holt* [2010] estimated the viscosity to lie in the range $\sim 10^{21}$ to 10^{22} Pa s for most of that region. Estimates of the effective viscosity of the Tibetan lithosphere lie in the range 5×10^{22} to 5×10^{21} Pa s at strain rates of 3 to 30 nanostrain per year [*England and Molnar*, 1997; *Flesch et al.*, 2001]. Estimates of the viscosity of the lithosphere in western North America lie in the range $\sim 10^{21}$ to 10^{22} Pa s [*e.g. Flesch et al.*, 2000; *Jones et al.*, 1996; *Townsend and Sonder*, 2001]. *D'Agostino et al.* [2014] obtained an estimate for the Apennines of 1.5 to 3×10^{21} Pa s at a strain rate of ~ 50 nanostrain per year, and *England and Molnar* [2015] estimated the effective viscosity of the of the Tien Shan to be 1 to 4×10^{22} at a strain rate of ~ 30 nanostrain per year.

The experiments summarised in Figures 6 and 7 place limits on the variations of the viscosity coefficient B within the Arabia-Eurasia convergence zone. Lateral variations in the effective viscosity by a factor of five or more arise within lithosphere with constant B (Figure 10), simply from the dependence of effective viscosity on deviatoric stress (Eq. (7)). These variations comfortably exceed the permitted variation of B' (Section 4.2), with the possible exception that the upper bound on B' for the Central Iranian plateau is effectively unconstrained.

The small permitted diminution in strength within the Turkish-Iranian plateau ($B' > 0.7$) may seem surprising, in view of the suggestion that the volcanism of the region represents loss of the lower lithosphere and its replacement by asthenosphere [*Şengör et al.*, 2003]. That process is envisaged, however, to involve only the weak, lower, part of the lithosphere [*e.g. Houseman et al.*, 1981; *Houseman and Molnar*, 1997; *Molnar et al.*,

1998] so, while loss of the lower lithosphere may appreciably increase the GPE of the remainder, it may not greatly alter its integrated strength [*e.g. England and Houseman*, 1989]. In contrast, the process of delamination is envisaged to remove the strong portion of the lithosphere [*e.g. Bird*, 1979; *Bird and Baumgardner*, 1981].

The tight constraint on B' for the Zagros (Figures 6 and 7) excludes the possibility that this region is significantly stronger than its surroundings, as might have been inferred from the high upper mantle wave speeds observed beneath the region. *Priestley et al.* [2012] argue, however, that the these high wave speeds represent thickening of the lithosphere as a result of the convergence between Arabia and Eurasia, so they need not imply that the region is strong. Indeed, the 1D analytical approximation (Figure 4) and the 2D numerical calculations (Figures 6 to 9) each require that the lithosphere of the Zagros must be weak enough to deform under the observed gradients of GPE.

B' for Central Iranian Plateau may be as low as 0.6, consistent with the observations of low wave speeds in the uppermost mantle of the region. An arbitrarily strong plateau is, however, permitted by the observations (Figure 6b, Figure 7) although the misfits for such solutions are negligibly different from those for spatially invariant physical properties. High values of B' are permitted because the deviatoric stress in this region is so low that its effective viscosity is already high (Figure 10) and further increasing B has very little influence on the velocity field. We therefore cannot rule out suggestions that the plateau is intrinsically strong ($B' \gg 1$) [*e.g. Jackson and M$^{\text{c}}$Kenzie*, 1988; *Sobouti and Arkani-Hamed*, 1996] but in view of the fact that it has undergone horizontal shortening during Tertiary time and is likely to be underlain by hot, weak uppermost mantle, it seems more reasonable to suggest that the plateau's present state of low strain rate is simply explained

by the fact that its GPE is high enough to resist the compressional stresses applied by its surroundings [*Hatzfeld and Molnar*, 2010].

5.3. Comparison with focal mechanisms of earthquakes

The agreement between the physical model and the strain rates determined from GPS velocities (Figure 9) suggests that the deformation in the convergence zone between Arabia and Eurasia is determined by the balance between gradients of gravitational potential energy and gradients of stress required to deform the lithosphere (Eq. (A6)). The geodetic strain rates are derived from measurements on the decadal time scale and reflect primarily inter-seismic deformation of the upper crust; the question arises, therefore, as to whether the same physical model can explain the longer-term deformation of the upper crust, which is primarily accommodated by earthquakes.

In testing the thin-sheet model, we have assumed that the style of deformation in the upper crust follows the ductile strain of the lower lithosphere. Under that assumption the expected style of faulting may be calculated from the principal axes of horizontal strain rate in the thin-sheet calculations [*Gordon and Houseman*, 2015; *Houseman and England*, 1986]. At any location the triaxial strain-rate field of the ductile layer is compatible with a pair of double couple mechanisms acting in the brittle layer. The quantity

$$p = \frac{3}{4} + \frac{1}{\pi} \arctan\left(\frac{\dot{\varepsilon}_2}{\dot{\varepsilon}_1}\right) \tag{14}$$

indicates the expected style of surficial faulting, where $\dot{\varepsilon}_1$ and $\dot{\varepsilon}_2$ are principal horizontal strain rates, and $\dot{\varepsilon}_1 \geq \dot{\varepsilon}_2$. When $0 \leq p \leq 0.25$ there is reverse faulting only (RR, Figure 11). When $0.25 \leq p \leq 0.5$ there is reverse faulting plus subsidiary strike slip (RS) or strike slip plus subsidiary reverse faulting (SR), with the transition between RS

and SR taking place where $p = 0.375$. Pure strike-slip faulting occurs when $p = 0.5$ and the transitions from strike-slip with subsidiary normal faulting (SN) to normal faulting with subsidiary strike-slip (NS) and from NS to NN (normal faulting only) take place at $p = 0.625$ and $p = 0.75$ (Figure 11).

The thin-sheet calculations show that faulting should lie mainly in the ranges of reverse faulting with subsidiary strike-slip (RS), or of strike-slip with subsidiary reverse (SR), with a small region of pure reverse faulting (RR) (Figure 11). We use earthquakes from the GCMT catalog [*Dziewonski et al.*, 1981; *Ekström et al.*, 2012] and separate them into reverse-, strike-slip-, or normal-faulting events according to whether the smallest, intermediate, or greatest principal axis of their moment tensor is closest to vertical. The regions corresponding to RR contain 7 earthquakes, of which 5 have reverse-faulting mechanisms and 2 have strike-slip mechanisms. In the regions where reverse faulting with subsidiary strike-slip is expected (RS), there are 141 reverse-faulting earthquakes, 58 strike-slip and 3 with normal-faulting mechanisms. In the regions where strike-slip with subsidiary reverse faulting is expected (SR), there are 113 strike-slip earthquakes, 89 reverse-faulting and 9 with normal-faulting mechanisms. The normal-faulting earthquakes in the RS and SR regions account for less than 1% of the moment release (SR) and less than 0.1% (RS), and probably represent stress heterogeneity associated with larger nearby earthquakes. Otherwise, the distribution of earthquake types is consistent with that predicted by the thin-sheet calculations, with reverse faulting dominating in RS regions, and strike-slip faulting dominating in SR regions.

The agreement between the style of deformation shown by our calculations and the distribution of earthquakes suggests that strains occurring in the ductile lithosphere are

compatible with deformation in the seismogenic upper crust. This observation validates a key assumption of the thin viscous sheet model: that vertical gradients of horizontal displacement maybe neglected when analysing the deformation of the lithosphere at the scale of tens to hundreds of kilometers. Many of the earthquakes in our region of study that have magnitudes greater than about 6 are associated with faults that show displacements of 100s of meters to kilometers over Quaternary time [*e.g. Berberian and Yeats*, 1999; *Fattahi et al.*, 2006; *Foroutan et al.*, 2012; *Le Dortz et al.*, 2009; *Meyer and Le Dortz*, 2007; *Meyer et al.*, 2006; *Nazari et al.*, 2009; *Shabanian et al.*, 2010; *Regard et al.*, 2005; *Talebian and Jackson*, 2002; *Walker and Jackson*, 2004; *Walker et al.*, 2010]. We therefore suggest that the Quaternary deformation of this convergent zone is characterised by the same balance between gradients of GPE and deviatoric stress that explains the decadal-scale deformation [see *Hatzfeld and Molnar*, 2010].

5.4. Implications for seismic hazard

Although the presence of large fault systems within the convergence zone (Figure 1) encourages a description of the kinematics in terms of the relative motions of rigid blocks that are separated by those fault systems [*e.g. Jackson and McKenzie*, 1988; *Reilinger et al.*, 2006; *Walpersdorf et al.*, 2014], the assumption of block-like behavior carries the risk of serious error in the analysis of seismic hazard. If all the fault zones capable of delivering damaging earthquakes are identified and correctly assigned to block boundaries, then block models may provide useful constraints on slip rates, and hence on the distribution of hazard. If, however, a block model were to be based upon an incomplete catalog of faulting then its use in seismic hazard estimation would be seriously misleading: hazard

would be over-estimated near the boundaries of the blocks, and underestimated in their interiors.

The analysis of the previous two subsections indicates that, while some regions deform more slowly than others, there is little evidence for rigid behavior. Though the strain-rates may be low, our inference that the brittle upper crust follows the ductile creep of the deforming lithosphere (Section 5.3) implies that the brittle upper layer will eventually attain stress differences that can cause earthquakes. A more prudent approach to the seismic hazard of the region may therefore be to seek a relationship between seismicity and strain rate [*e.g. Bird et al.*, 2010, 2015]. To investigate this suggestion we compared the seismic moment release since AD 1900 with the distribution of strain rate calculated from GPS measurements. Figure 12 shows the epicenters of earthquakes [*Ambraseys and Melville*, 1982; *Dziewonski et al.*, 1981; *Ekström et al.*, 2012; *Engdahl and Villaseñor*, 2002] superimposed on the second invariant of the strain rate calculated from GPS. Although the epicenters are more abundant in regions in which the strain rate is higher than 20 nanostrain/yr, dozens of earthquakes occurred in regions having strain rates lower than 10 nanostrain per year. Only the southwestern Central Iranian Plateau (around 54°E, 31°N), the largest region in which strain rate is lower than ∼10 nanostrain/yr, is aseismic on the historical time scale.

We next calculated the second invariant of the strain rate from the GPS observations (Section A1) in 100×100 km boxes, and summed the scalar moments of the earthquakes within each box, using the GCMT catalog [*Dziewonski et al.*, 1981; *Ekström et al.*, 2012] for the interval from 1976 to 2014 and the catalog of *Engdahl and Villaseñor* [2002] for the interval 1900 to 1975. Figure 12b shows the cumulative seismic moment in these boxes,

plotted in ascending order of strain rate in the box. Approximately half of the seismic moment release took place within areas where the calculated strain rate is between 5 and 20 nanostrain/year, with the rest taking place in regions where the strain rates lie between 20 and ∼50 nanostrain/yr (Figure 12b).

Although the Central Iranian Plateau has been relatively aseismic in recent time (Figure 12a), there were significant historical earthquakes in the Plateau [*Ambraseys and Melville*, 1982]. Furthermore, the region is cut by several faults over 100 km in length which generally have time-averaged slip rates of lower than 1 mm/yr, but show clear evidence of earthquakes in Holocene time [*e.g. Foroutan et al.*, 2012; *Le Dortz et al.*, 2009, 2011; *Meyer and Le Dortz*, 2007; *Meyer et al.*, 2006; *Nazari et al.*, 2009]. Similarly, parts of north-eastern Iran (around 57°E, 37°E) and northwestern Iran (around 48°E, 40°E) that are 2–300 km on a side had few earthquakes since the beginning of the twentieth century and have strain rates lower than about 20 nanostrain per year. The historical catalog [*Ambraseys and Melville*, 1982] shows, however, abundant earthquakes in those regions (Figure 12a). These observations suggest that the entire region may be susceptible to seismic hazard on faults that have low slip rates and long recurrence intervals, a situation that is common in regions of continental deformation [*e.g. England and Jackson*, 2011; *Zhang*, 2013]. The construction of a denser field of crustal velocities, either from GPS or InSAR, is essential to the better assessment of seismic hazard in Iran and neighboring regions.

6. Conclusion

A model that treats the lithosphere as a thin sheet with spatially invariant viscosity coefficient fits the observed velocity distribution with a RMS misfit of 2.4 mm/yr, a 95%

reduction in variance (Section 4.1). Allowing lateral heterogeneity in material properties produces negligible reduction in misfits (Section 4.2, Figure 6, and Table 2). While the hypothesis that the Central Iranian Plateau is considerably stronger than its surroundings cannot be ruled out, this condition is not required by the available GPS measurements (Section 4.2). It seems more likely that the low strain rate of the plateau is explained by a state of low deviatoric stress as its high GPE balances the compressional stresses applied to the region [see discussion of Figures 4, 9, and 12, and *Hatzfeld and Molnar*, 2010]. A denser and more precise field of velocity is required to resolve whether more complex configurations of rheology are demanded by the observations. We conclude that the balance between gravitational potential energy and the stress required to deform the lithosphere shapes the deformation field of Iran, and controls the distribution of active faults, seismicity and seismic hazard across the region.

Appendix A: Appendix

A1. Calculation of strain-rate tensor from GPS velocities

We calculate strain rates from the GPS velocities using the method of *Shen et al.* [2015] in which the horizontal velocity gradients are estimated at a set of regularly spaced gridpoints from the weighted GPS velocities by least-squares inversion. The weight on each observation is the product of the area of the Voronoi cell occupied by the site and a Gaussian weight, $\exp\left(-R_{ij}^2/D_j^2\right)$, where R_{ij} is the distance of site i from gridpoint j. The smoothing distances, D_j, at the gridpoints are chosen so that the total weight of observations (W_T in the notation of *Shen et al.* [2015]) is the same for each gridpoint. The significance of W_T lies in the distribution of D_j that it produces for a given data set. In the body of the text we set that weight to 35, which translates into a median smoothing distance of 160 km (Figure 2 and Figures 9 to 12). Figure 13 shows the influence of changing the choice of weight upon the distribution of smoothing distances. A weight of 20 translates into a median smoothing distance of 120 km, and produces strain rates in regions of denser GPS coverage that are up to 50% higher than in the fields with weight equal to 35 that we use in the body of the paper (Figure 13c). A weight of 47.5 translates into a median smoothing distance of 200 km, and produces strain rates in regions of denser GPS coverage that are up to 25% lower than in the fields with weight equal to 35 (Figure 13e). The azimuths of the axes of principal horizontal compression generally vary by less than 10° for the different choices of weight (Figure 13d, f.)

A2. Numerical solutions to thin-sheet equation

The thin-sheet approximation assumes that vertical tractions on vertical planes may be neglected, so that density variations within the lithosphere are in local isostatic balance.

Under this condition, the stress balance equation for creeping flow in spherical coordinates is:

$$\frac{2}{r}\frac{\partial \overline{\tau}_{\theta\theta}}{\partial \theta} + \frac{1}{r}\frac{\partial \overline{\tau}_{\phi\phi}}{\partial \theta} + \frac{1}{r\sin\theta}\frac{\partial \overline{\tau}_{\theta\phi}}{\partial \phi} + \frac{\cot\theta}{r}\left(\overline{\tau}_{\theta\theta} - \overline{\tau}_{\phi\phi}\right) = \frac{1}{rL}\frac{\partial \Gamma}{\partial \theta}$$

$$\frac{1}{r\sin\theta}\frac{\partial \overline{\tau}_{\theta\theta}}{\partial \phi} + \frac{2}{r\sin\theta}\frac{\partial \overline{\tau}_{\phi\phi}}{\partial \phi} + \frac{1}{r}\frac{\partial \overline{\tau}_{\theta\phi}}{\partial \theta} + \frac{2\cot\theta}{r}\overline{\tau}_{\theta\phi} = \frac{1}{r\sin\theta L}\frac{\partial \Gamma}{\partial \phi} \qquad (A1)$$

where θ and ϕ are respectively the co-latitude and the longitude (in radians) and r is the radial distance from the center of the earth, L is the thickness of the lithosphere, and Γ is the gravitational potential energy per unit area of lithosphere (GPE) [*Bird and Piper*, 1980; *England and McKenzie*, 1983; *Gordon and Houseman*, 2015; *Houseman and England*, 1986]. These equations are non-dimensionalized using the lithospheric thickness, L, as a scale length and using a scale velocity, U_0:

$$\dot{\varepsilon}'_{ij} = \dot{\varepsilon}_{ij}\frac{L}{U_0} \qquad (A2)$$

$$\overline{\tau}'_{ij} = \frac{\overline{\tau}_{ij}}{B\left(U_0/L\right)^{1/n}} \qquad (A3)$$

$$\Gamma' = \frac{\Gamma}{g\rho_c L^2(1 - \rho_c/\rho_m)} \qquad (A4)$$

and all variables are identified in Table 3.

This non-dimensionalisation allows us to express the rheology of the thin sheet by two parameters, n the power-law exponent, and the Argand number

$$Ar = \frac{g\rho_c(1 - \rho_c/\rho_m)L}{B(U_0/L)^{1/n}} \qquad (A5)$$

England and McKenzie [1982]. In presenting our calculations in dimensional form we use the values of g, ρ_c, ρ_m, U_0 and L given in Table 3. The value of U_0 is set here to 30 mm/yr, but the best-fit value of Ar varies inversely with U_0, so that the implied physical value of B is independent of the choice of U_0.

A3. Analytical Solution in one dimension

In Section 3 we consider a cross-section through Iran, along which it is reasonable to treat the velocity as varying only in the along-strike (x-)direction. Under this condition, the equation of stress balance reduces to

$$\frac{\mathrm{d}\overline{\tau}_{xx}}{\mathrm{d}x} = \frac{1}{2L}\frac{\mathrm{d}\Gamma}{\mathrm{d}x}. \tag{A6}$$

[*D'Agostino et al.*, 2014; *Dalmayrac and Molnar*, 1981]. The deviatoric stress is related to horizontal strain rate by

$$\overline{\tau}_{xx} = 2\eta_{\mathrm{eff}}\dot{\varepsilon}_{xx}, \tag{A7}$$

where

$$\dot{\varepsilon}_{xx} = \frac{\mathrm{d}u_x}{\mathrm{d}x}, \tag{A8}$$

u_x is the component of horizontal velocity in the direction of the profile and η_{eff} is the vertically-averaged effective viscosity of the lithosphere.

We assume that the effective viscosity is constant along the profile; *D'Agostino et al.* [2014] show that the differences between solutions obtained for a Newtonian thin sheet (η_{eff} constant) and those for a power-law thin sheet with $n > 1$ (η_{eff} varying with strain rate, Eq. 9) are small, because the variations in strain rate occur over length scales that are primarily controlled by the variations in topography. For lithosphere of spatially invariant physical properties, Eq. (A6) may be integrated twice to yield a relation between the velocity in the direction perpendicular to the chain and the integral, in the same direction, of the GPE [*D'Agostino et al.*, 2014]. We consider a mountain belt of width W and constant effective viscosity, η_{eff}, with the velocities at either end of the profiles being

U_1 and U_2. Eq. (A6), when combined with Eqs. (A7) and (A8), becomes

$$\frac{\mathrm{d}^2 u_x}{\mathrm{d}x^2} = \frac{1}{4\eta_{\mathrm{eff}} L} \frac{\mathrm{d}\Gamma}{\mathrm{d}x} \tag{A9}$$

Integrating twice, we obtain

$$u_x = \frac{1}{4\eta_{\mathrm{eff}} L} \int_0^x \Delta\Gamma(x')\mathrm{d}x' + Cx + D, \tag{A10}$$

where $\int_0^x \Delta\Gamma(x')\mathrm{d}x'$ is the integral along the profile of the difference between the GPE of the lithosphere and that at $x = 0$. The boundary conditions $U(0) = U_1; U(W) = U_2$ give

$$u_x = U_1 + \frac{(U_2 - U_1)\,x}{W} + \frac{1}{4\eta_{\mathrm{eff}} L}\left[\int_0^x \Delta\Gamma(x')\mathrm{d}x' - \frac{x}{W}\int_0^W \Delta\Gamma(x')\mathrm{d}x'\right]. \tag{A11}$$

[*England and Molnar*, 2015].

References

Aktuğ, B., E. Meherremov, M. Kurt, S. Özdemir, N. Esedov, and O. Lenk (2013a), GPS constraints on the deformation of Azerbaijan and surrounding regions, *Journal of*

Geodynamics, *67*, 40–45, doi:10.1016/j.jog.2012.05.007.

Aktuğ, B., U. Dikmen, A. Dogru, and H. Ozener (2013b), Seismicity and strain accumulation around Karliova triple junction (Turkey), *Journal of Geodynamics*, *67*, 21–29, doi:10.1016/j.jog.2012.04.008.

Al-Lazki, A. I., D. Seber, E. Sandvol, N. Türkelli, R. Mohamad, and M. Barazangi (2003), Tomographic Pn velocity and anisotropy structure beneath the Anatolian plateau (eastern Turkey) and the surrounding regions, *Geophysical Research Letters*, *30*(24), n/a–n/a.

Al-Lazki, A. I., E. Sandvol, D. Seber, M. Barazangi, N. Türkelli, and R. Mohamad (2004), Pn tomographic imaging of mantle lid velocity and anisotropy at the junction of the Arabian, Eurasian and African plates, *Geophysical Journal International*, *158*(3), 1024–1040.

Al-Lazki, A. I., K. S. Al-Damegh, S. Y. El-Hadidy, A. Ghods, and M. Tatar (2014), Pn-velocity structure beneath Arabia-Eurasia Zagros collision and Makran subduction zones, *Geological Society London Special Publications*, *392*(1), 45–60.

Alinaghi, A., I. Koulakov, and H. Thybo (2007), Seismic tomographic imaging of P- and S-waves velocity perturbations in the upper mantle beneath Iran, *Geophysical Journal International*, *169*(3), 1089–1102.

Ambraseys, N., and R. Bilham (2003), Earthquakes in Afghanistan, *Seismological Research Letters*, *74*(2), 107–123.

Ambraseys, N., and C. Melville (1982), *A History of Persian Earthquakes*, Cambridge University Press, Cambridge.

Amini, S., Z. H. Shomali, H. Koyi, and R. G. Roberts (2012), Tomographic upper-mantle velocity structure beneath the Iranian Plateau, *Tectonophysics*, *554-557*, 42–49.

Baker, C., J. Jackson, and K. Priestley (1993), Earthquakes on the Kazerun Line in the Zagros Mountains of Iran - Strike-Slip Faulting Within a Fold-and-Thrust Belt, *Geophysical Journal International*, *115*(1), 41–61.

Berberian, M., and R. S. Yeats (1999), Patterns of historical earthquake rupture in the Iranian Plateau, *Bull. Seismol. Soc. Amer.*, *89*, 120–139.

Bird, P. (1979), Continental delamination and the Colorado Plateau, *J. Geophys. Res.*, *84*, 7561–7571.

Bird, P., and J. Baumgardner (1981), Steady propagation of delamination events, *J. Geophys. Res.*, *86*, 4891–4903.

Bird, P., and K. Piper (1980), Plane-stress finite-element models of tectonic flow in southern California, *Phys. Earth Planet Inter.*, *21*, 158–175.

Bird, P., C. Kreemer, and W. E. Holt (2010), A long-term forecast of shallow seismicity based on the global strain rate map, *Seismological Research Letters*, *81*(2), 184–194, doi:10.1785/gssrl.81.2.184.

Bird, P., D. D. Jackson, Y. Y. Kagan, C. Kreemer, and R. s. Stein (2015), GEAR1: A Global Earthquake Activity Rate Model Constructed from Geodetic Strain Rates and Smoothed Seismicity, *Bulletin Of The Seismological Society Of America*, *105*(5), 2538–2554.

Bourne, S., P. England, and B. Parsons (1998), The motion of crustal blocks driven by flow of the lower lithosphere and implications for slip rates of continental strike-slip faults, *Nature*, *391*, 655–659.

Chase, C., J. Libarkin, and A. Sussman (2002), Colorado Plateau: Geoid and means of isostatic support, *International Geology Review*, *44*(7), 575–587.

Copley, A., and J. Jackson (2006), Active tectonics of the Turkish-Iranian plateau, *Tectonics*, *25*(6).

D'Agostino, N., P. England, I. Hunstad, and G. Selvaggi (2014), Gravitational potential energy and deformation of the Apennines, *Earth Planetary Science Lett.*, *397*, 121–132, doi:10.1016/j.epsl.2014.04.013.

Dalmayrac, B., and P. Molnar (1981), Parallel thrust and normal faulting in Peru and constraints on the state of stress, *Earth Planet. Sci. Lett.*, *55*(3), 473–481.

Djamour, Y., P. Vernant, R. Bayer, H. R. Nankali, J.-F. Ritz, J. Hinderer, Y. Hatam, B. Luck, N. Le Moigne, M. Sedighi, and F. Khorrami (2010), GPS and gravity constraints on continental deformation in the Alborz mountain range, Iran, *Geophys. J. Int*, *183*, 1287–1301.

Djamour, Y., P. Vernant, H. R. Nankali, and F. Tavakoli (2011), NW Iran-eastern Turkey present-day kinematics: Results from the Iranian permanent GPS network, *Earth Planet. Sci. Lett.*, *307*, 27–34, doi:10.1016/j.epsl.2011.04.029.

Dziewonski, A. M., T.-A. Chou, and J. H. Woodhouse (1981), Determination of earthquake source parameters from waveform data for studies of global and regional seismicity, *J. Geophys. Res.*, *86*, 2825–2852.

Ekström, G., M. Nettles, and A. Dziewonski (2012), The Global CMT Project 2004–2010: centroid-moment tensors for 13,017 earthquakes, *Phys. Earth Planet Inter.*, *200-201*, 1–9.

Engdahl, E. R., and A. Villaseñor (2002), Global seismicity: 1900–1999, in *IASPEI Handbook of Earthquake and Engineering Seismology, Part A*, edited by W. H. K. Lee, P. Jennings, H. Kanamori, and C. Kisslinger, pp. 665–690, Academic Press, Boston.

Engdahl, E. R., J. A. Jackson, S. C. Myers, E. A. Bergman, and K. Priestley (2006), Relocation and assessment of seismicity in the Iran region, *Geophys. J. Int.*, *167*, 761–778.

England, P., and G. Houseman (1989), Extension during continental convergence, with application to the Tibetan plateau, *J. Geophys. Res.*, *94*, 17,561–17,579.

England, P., and J. A. Jackson (2011), Uncharted seismic risk, *Nature GeoScience*, *4*, 348–349, doi:doi:10.1038/ngeo1168.

England, P., and D. McKenzie (1982), A thin viscous sheet model for continental deformation, *Geophys. J. Royal Astron. Soc.*, *70*, 295–321.

England, P., and D. McKenzie (1983), Correction to a thin viscous sheet model for continental deformation, *Geophys. J. Royal Astron. Soc.*, *73*, 523–532.

England, P., and P. Molnar (1997), Active deformation of Asia: From kinematics to dynamics, *Science*, *278*, 647–650.

England, P., and P. Molnar (2015), Rheology of the lithosphere beneath the central and western Tien Shan, *J. Geophys. Res.*, *120*, 3803—3823, doi:10.1002/2014JB011733.

England, P., G. Houseman, and L. Sonder (1985), Length scales for continental deformation in convergent, divergent and strike-slip environments: analytical and approximate solutions for a thin viscous sheet model, *J. Geophys. Res.*, *90*, 3,551–3,557.

England, P., G. Houseman, and J.-M. Nocquet (2016), Constraints from GPS observations on the balance of forces in the deformation of Anatolia and the Aegean, *J. Geophys.*

Res, *121*, doi:10.1002/2016JB013382, 2016JB013382.

Farr, T., P. Rosen, E. Caro, R. Crippen, R. Duren, S. Hensley, M. Kobrick, M. Paller, E. Rodríguez, and L. Roth (2007), The Shuttle Radar Topography Mission, *Rev. Geophys.*, *45*(RG2004), doi:10.1029/2005RG000183.

Fattahi, M., R. Walker, J. Hollingsworth, A. Bahroudi, H. Nazari, M. Talebian, S. Armitage, and S. Stokes (2006), Holocene slip-rate on the Sabzevar thrust fault, NE Iran, determined using optically stimulated luminescence (OSL), *Earth And Planetary Science Letters*, *245*(3-4), 673–684.

Flesch, L., A. Haines, and W. Holt (2001), Dynamics of the India-Eurasia collision zone, *J. Geophys. Res.*, *106*(B8), 16,435–16,460.

Flesch, L. M., W. E. Holt, A. J. Haines, and T. B. Shen (2000), Dynamics of the Pacific-North American plate boundary in the Western United States, *Science*, *287*(5454), 834–836.

Foroutan, M., M. Sébrier, H. Nazari, B. Meyer, M. Fattahi, A. Rashidi, K. Le Dortz, and M. D. Bateman (2012), New evidence for large earthquakes on the Central Iran plateau: palaeoseismology of the Anar fault, *Geophysical Journal International*, *189*, 6–18, doi:10.1111/j.1365-246X.2012.05365.x.

Frank, F. C. (1972), Plate tectonics, the analogy with glacier flow and isostasy, in *Flow and fracture of rocks: AGU Monograph 16*, edited by H. C. Heard, I. Y. Borg, N. L. Carter, and C. B. Raleigh, pp. 285–292, Amer. Geophys. Union.

Gordon, R. G., and G. A. Houseman (2015), Deformation of Indian Ocean lithosphere: Evidence for a highly nonlinear rheological law, *J. Geophys. Res. Solid Earth*, *120*, 4434–4449, doi:10.1002/2015JB011993.

Hammond, W. C., G. Blewitt, and C. Kreemer (2011), Block modeling of crustal deformation of the northern Walker Lane and Basin and Range from GPS velocities, *J. of Geophys. Res.*, *116*(B4), B04,402.

Hatzfeld, D., and P. Molnar (2010), Comparisons of the kinematics and deep structures of the Zagros and Himalaya and of the Iranian and Tibetan plateaus and geodynamic implications, *Reviews of Geophysics*, *48*(2), RG2005–48.

Haxby, W. F., and D. L. Turcotte (1978), On isostatic geoid anomalies, *J. Geophys. Research, A, Space Physics*, *83*(B11), 5473–5478.

Hessami, K., F. Nilforoushan, and C. Talbot (2006), Active deformation within the Zagros Mountains deduced from GPS measurements, *J. Geol. Soc. Lond.*, *163*, 143–148.

Hollingsworth, J., J. Jackson, R. Walker, M. R. Gheitanchi, and M. J. Bolourchi (2006), Strike-slip faulting, rotation, and along-strike elongation in the Kopeh Dagh mountains, NE Iran, *Geophys. J. Int.*, *166*, 1161–1177.

Hollingsworth, J., M. Fattahi, R. Walker, M. Talebian, A. Bahroudi, M. J. Bolourchi, J. Jackson, and A. Copley (2010), Oroclinal bending, distributed thrust and strike-slip faulting, and the accommodation of Arabia-Eurasia convergence in NE Iran since the Oligocene, *Geophys. J. Int.*, *181*, 1214–1216.

Houseman, G., and P. England (1986), Finite strain calculations of continental deformation 1. Method and general results for convergent zones, *J. Geophys. Res.*, *91*(B3), 3651–3663.

Houseman, G., and P. Molnar (1997), Gravitational (Rayleigh–Taylor) instability of a layer with non-linear viscosity and convective thinning of continental lithosphere, *Geophys. J. Int*, *128*, 125–150.

Houseman, G., D. McKenzie, and P. Molnar (1981), Convective instability of a thickened boundary layer and its relevance for the thermal evolution of continental convergent belts, *J. Geophys. Res.*, *86*, 6115–6132.

Innocenti, F., R. Mazzuoli, G. Pasquare, F. Radicati Di Brozolo, and L. Villari (1976), Evolution of volcanism in area of interaction between Arabian, Anatolian and Iranan plates (Lake Van, Eastern Turkey), *J. Volcanol. Geotherm. Res.*, pp. 103–112.

Jackson, J., and D. McKenzie (1984), Active tectonics of the Alpine-Himalayan Belt between western Turkey and Pakistan, *Geophys. J. R. Astron. Soc.*, *77*, 185–264.

Jackson, J., and D. P. McKenzie (1988), The relationship between plate motions and seismic moment tensors and the rate of active deformation in the Mediterranean and Middle East, *Geophys. J. R. Astr. Soc.*, *93*, 45–73.

Jackson, J., K. Priestley, M. Allen, and M. Berberian (2002), Active tectonics of the south Caspian basin, *Geophys. J. Int.*, *148*, 214–245.

Javidfakhr, B., O. Bellier, E. Shabanian, S. Ahmadian, and A. Saidi (2011), Plio–Quaternary tectonic regime changes in the transition zone between Alborz and Kopeh Dagh mountain ranges (NE Iran), *Tectonophysics*, *506*, 86–108, doi: 10.1016/j.tecto.2011.04.013.

Jones, C., J. Unruh, and L. Sonder (1996), The role of gravitational potential energy in active deformation in the southwestern United States, *Nature*, *391*, 37–41.

Kadirov, F., M. Floyd, A. Alizadeh, I. Guliev, R. Reilinger, S. Kuleli, R. King, and M. N. Toksoz (2012), Kinematics of the eastern Caucasus near Baku, Azerbaijan, *Nat. Haz.*, *63*, 997–1006.

Karakhanyan, A., P. Vernant, E. Doerflinger, A. Avagyan, H. Philip, R. Aslanyan, C. Champollion, S. Arakelyan, P. Collard, H. Baghdasaryan, M. Peyret, V. Davtyan, E. Calais, and F. Masson (2013), GPS constraints on continental deformation in the Armenian region and Lesser Caucasus, *Tectonophys.*, *592*, 39–45.

Kaviani, A., A. Paul, E. Bourova, D. Hatzfeld, H. Pedersen, and M. Mokhtari (2007), A strong seismic velocity contrast in the shallow mantle across the Zagros collision zone (Iran), *Geophysical Journal International*, *171*(1), 399–410.

Kreemer, C., G. Blewitt, and E. C. Klein (2014), A geodetic plate motion and Global Strain Rate Model, *Geochemistry, Geophysics, Geosystems*, *15*(10), 3849–3889.

Le Dortz, K., B. Meyer, M. Sébrier, H. Nazari, R. Braucher, M. Fattahi, L. Benedetti, M. Foroutan, L. Siame, D. Bourlès, M. Talebian, M. D. Bateman, and M. Ghoraishi (2009), Holocene right-slip rate determined by cosmogenic and OSL dating on the Anar fault, Central Iran, *Geophys. J. Int.*, *179*(2), 700–710.

Le Dortz, K., B. Meyer, M. Sébrier, R. Braucher, H. Nazari, L. Benedetti, M. Fattahi, D. Bourlès, M. Foroutan, L. Siame, A. Rashidi, and M. D. Bateman (2011), Dating inset terraces and offset fans along the Dehshir Fault (Iran) combining cosmogenic and OSL methods, *Geophysical Journal International*, *185*(3), 1147–1174.

Maggi, A., and K. Priestley (2005), Surface waveform tomography of the Turkish-Iranian plateau, *Geophys J Int*, *160*(3), 1068–1080.

Masson, F., J. Chery, D. Hatzfeld, J. Martinod, P. Vernant, F. Tavakoli, and M. Ghafory-Ashtiani (2005), Seismic versus aseismic deformation in Iran inferred from earthquakes and geodetic data, *Geophys. J. Int.*, *160*(1), 217–226.

Masson, F., M. Anvari, Y. Djamour, A. Walpersdorf, F. Tavakoli, M. Daignières, H. Nankali, and S. Van Gorp (2007), Large-scale velocity field and strain tensor in Iran inferred from GPS measurements: new insight for the present-day deformation pattern within NE Iran, *Geophysical Journal International*, *170*, 436–440.

Masson, F., M. Lehujeur, Y. Ziegler, and C. Doubre (2014), Strain rate tensor in Iran from a new GPS velocity field, *Geophys. J. Int.*, *197*, 10–21, doi:10.1093/gji/ggt509.

McKenzie, D. (1970), Plate tectonics of the Mediterranean region, *Nature*, *226*(5242), 239–243.

McKenzie, D. (1972), Active tectonics of the Mediterranean region, *Geophys. J. Royal Astron. Soc.*, *30*(2), 109–185.

Meade, B. J., and B. H. Hager (2005), Block models of crustal motion in southern California constrained by GPS measurements, *J. Geophys. Res.*, *110*, doi:10.1029/2004JB003,209.

Meade, B. J., B. H. Hager, S. C. McClusky, R. E. Reilinger, S. Ergintav, O. Lenk, A. Barka, and H. Özener (2002), Estimates of seismic potential in the Marmara Sea region from block models of secular deformation constrained by Global Positioning System measurements, *Bull. Seismol. Soc. Amer.*, *92*(1), 208–215.

Meyer, B., and K. Le Dortz (2007), Strike-slip kinematics in Central and Eastern Iran: Estimating fault slip-rates averaged over the Holocene, *Tectonics*, *26*(5), TC5009.

Meyer, B., F. Mouthereau, O. Lacombe, and P. Agard (2006), Evidence of Quaternary activity along the Deshir Fault: implication for the Tertiary tectonics of Central Iran, *Geophysical Journal International*, *164*(1), 192–201.

Molnar, P. (1988), Continental tectonics in the aftermath of plate tectonics, *Nature*, *335*(6186), 131–137.

Molnar, P., and H. Lyon-Caen (1988), Some simple physical aspects of the support, structure, and evolution of mountain belts, in *Processes in Continental Lithospheric Deformation*, vol. 218, edited by S. P. Clark, Jr., B. C. Burchfiel, and J. Suppe, pp. 179–207, The Geological Society of America.

Molnar, P., and P. Tapponnier (1978), Active tectonics of Tibet, *J. Geophys. Res.*, *83*, 2648–2682.

Molnar, P., P. England, and J. Martinod (1993), Mantle dynamics, uplift of the Tibetan plateau, and the Indian monsoon, *Reviews of Geophysics*, *31*, 357–396.

Molnar, P., G. Houseman, and C. Conrad (1998), Rayleigh–Taylor instability and convective thinning of mechanically thickened lithosphere: effects of non-linear viscosity decreasing exponentially with depth and of horizontal shortening of the layer, *Geophysical Journal International*, *133*(3), 568–584.

Mousavi, Z., A. Walpersdorf, R. T. Walker, F. Tavakoli, E. Pathier, H. Nankali, F. Nilfouroushan, and Y. Djamour (2013), Global Positioning System constraints on the active tectonics of NE Iran and the South Caspian region, *Earth Planet. Sci. Lett.*, *377-378*, 287–298, doi:10.1016/j.epsl.2013.07.007.

Mutlu, A. K., and H. Karabulut (2011), Anisotropic Pn tomography of Turkey and adjacent regions, *Geophysical Journal International*, *187*(3), 1743–1758.

Nazari, H., M. Fattahi, B. Meyer, M. Sébrier, M. Talebian, M. Foroutan, K. Le Dortz, M. D. Bateman, and M. Ghorashi (2009), First evidence for large earthquakes on the Deshir Fault, Central Iran Plateau, *Terra Nova*, *21*(6), 417–426.

Özeren, M., and W. Holt (2010), The dynamics of the eastern Mediterranean and eastern Turkey, *Geophysical Journal International*, *183*(3), 1165–1184.

Parsons, B., and F. Richter (1980), A relation between the driving force and geoid anomaly associated with mid-ocean ridges, *Earth Planet. Sci. Lett.*, *51*(2), 445–450.

Pavlis, N. K., S. A. Holmes, S. C. Kenyon, and J. K. Factor (2012), The development and evaluation of the Earth Gravitational Model 2008 (EGM2008), *Journal of Geophysical Research*, *117*(B4), B04,406, doi:10.1029/2011JB008916.

Peyret, M., Y. Djamour, K. Hessami, V. Regard, O. Bellier, P. Vernant, M. Daignières, H. Nankali, S. V. Gorp, M. Goudarzi, J. Chéry, R. Bayer, and M. Rigoulay (2009), Present-day strain distribution across the Minab-Zendan-Palami fault system from dense GPS transects, *Geophysical Journal International*, *179*(2), 751–762.

Press, W., S. Teukolsky, W. Vetterling, and B. Flannery (1992), *Numerical Recipes: The Art of Scientific Computing*, second ed., Cambridge University Press, Cambridge.

Priestley, K., D. Mckenzie, J. Barron, M. Tatar, and E. Debayle (2012), The Zagros core: Deformation of the continental lithospheric mantle, *Geochemistry, Geophysics, Geosystems*, *13*, Q11,014.

Regard, V., O. Bellier, J. C. Thomas, D. Bourlès, S. Bonnet, M. R. Abbassi, R. Braucher, J. Mercier, E. Shabanian, S. Soleymani, and K. Feghhi (2005), Cumulative right-lateral fault slip rate across the Zagros-Makran transfer zone: role of the Minab-Zendan fault system in accommodating Arabia-Eurasia convergence in southeast Iran, *Geophysical Journal International*, *162*(1), 177–203.

Reilinger, R., and S. McClusky (2011), Nubia-Arabia-Eurasia plate motions and the dynamics of Mediterranean and Middle East tectonics, *Geophysical Journal International*,

186, 971–979.

Reilinger, R., S. McClusky, P. Vernant, S. Lawrence, S. Ergintav, R. Cakmak, H. Özener, F. Kadirov, I. Guliev, R. Stepanyan, M. Nadariya, G. Hahubia, S. Mahmoud, K. Sakr, A. ArRajehi, D. Paradissis, A. Al-Aydrus, M. Prilepin, T. Guseva, E. Evren, A. Dmitrotsa, S. V. Filikov, F. Gomez, R. Al-Ghazzi, and G. Karam (2006), GPS constraints on continental deformation in the Africa-Arabia-Eurasia continental collision zone and implications for the dynamics of plate interactions, *J. Geophys. Res.*, *111*(B10), B05411.

Şengör, A., S. Özeren, T. Genç, and E. Zor (2003), East Anatolian high plateau as a mantle supported, north-south shortened domal structure, *Geophysical Research Letters*, *30*(24).

Shabanian, E., O. Bellier, L. Siame, N. Arnaud, M. R. Abbassi, and J.-J. Cochemé (2009), New tectonic configuration in NE Iran: Active strike-slip faulting between the Kopeh Dagh and Binalud mountains, *Tectonics*, *28*(5), 1–29.

Shabanian, E., O. Bellier, M. R. Abbassi, L. Siame, and Y. Farbod (2010), Plio-Quaternary stress states in NE Iran: Kopeh Dagh and Allah Dagh-Binalud mountain ranges, *Tectonophysics*, *480*(1-4), 280–304.

Shen, Z.-K., M. Wang, Y. Zeng, and F. Wang (2015), Optimal interpolation of spatially discretized geodetic data, *Bull. Seismol. Soc. Amer.*, *105*(4), 2117–2127.

Siebert, L., and T. Simkin (2002), Volcanoes of the world: an illustrated catalog of Holocene volcanoes and their eruptions., Smithsonian Institution Digital Information Series GVP-3.

Sobouti, F., and J. Arkani-Hamed (1996), Numerical modelling of the deformation of the Iranian plateau, *Geophysical Journal International*, *126*(3), 805–818.

Talebian, M., and J. Jackson (2002), Offset on the Main Recent Fault of NW Iran and implications for the late Cenozoic tectonics of the Arabia-Eurasia collision zone, *Geophys. J. Int.*, *150*(2), 422–439.

Tatar, M., D. Hatzfeld, and M. Ghafory-Ashtiany (2004), Tectonics of the Central Zagros (Iran) deduced from microearthquake seismicity, *Geophysical Journal International*, *156*(2), 255–266.

Tatar, O., F. Poyraz, H. Gürsoy, Z. Cakir, S. Ergintav, Z. Akpnar, F. Koçbulut, F. Sezen, T. Türk, K. Ö. Hastaoğlu, A. Polat, B. L. Mesci, Ö. Gürsoy, İ. E. Ayazl, R. Çakmak, A. Belgen, and H. Yavaşoğlu (2012), Crustal deformation and kinematics of the eastern part of the North Anatolian Fault zone (Turkey) from GPS measurements, *Tectonophysics*, *518-521*, 55–62, doi:doi:10.1016/j.tecto.2011.11.010.

Tavakoli, F., A. Walpersdorf, C. Authemayou, H. R. Nankali, D. Hatzfeld, M. Tatar, Y. Djamour, F. Nilforoushan, and N. Cotte (2008), Distribution of the right-lateral strike–slip motion from the Main Recent Fault to the Kazerun Fault sytm (Zagros, Iran): Evidence from present-day GPS velocities, *Earth Planet. Sci. Lett.*, *275*(3-4), 342–347, doi:10.1016/j.epsl.2008.08.030.

Townsend, D., and L. Sonder (2001), Rheologic control of buoyancy-driven extension of the rio grande rift, *J. Geophys. Research*, *106*, 16.

Vernant, P., F. Nilforoushan, D. Hatzfeld, M. R. Abbassi, C. Vigny, F. Masson, H. Nankali, J. Martinod, A. Ashtiani, R. Bayer, F. Tavakoli, and J. Chéry (2004), Present-day crustal deformation and plate kinematics in the Middle East constrained by GPS mea-

surements in Iran and northern Oman, *Geophys. J. Int.*, *157*, 381–398.

Walker, R., and J. Jackson (2004), Active tectonics and late Cenozoic strain distribution in central and eastern Iran, *Tectonics*, *23* (TC5010).

Walker, R., M. Talebian, R. Sloan, A. Rasheedi, M. Fattahi, and C. Bryant (2010), Holocene slip-rate on the Gowk strike-slip fault and implications for the distribution of tectonic strain in eastern Iran, *Geophys. J. Int.*, doi:10.1111/j.1365-246X.2010.04538.x.

Walker, R. T., P. Gans, M. B. Allen, J. Jackson, M. Khatib, N. Marsh, and M. Zarrinkoub (2009), Late Cenozoic volcanism and rates of active faulting in eastern Iran, *Geophys. J. Int.*, *177*(2), 783–805.

Wallace, L. M., J. Beavan, R. McCaffrey, K. Berryman, and P. Denys (2007), Balancing the plate motion budget in the South Island, New Zealand using GPS, geological and seismological data, *Geophys J Int*, *168*(1), 332–352.

Walpersdorf, A., D. Hatzfeld, H. Nankali, F. Tavakoli, F. Nilforoushan, M. Tatar, P. Vernant, J. Chery, and F. Masson (2006), Difference in the GPS deformation pattern of North and Central Zagros (Iran), *Geophysical Journal International*, *167*(3), 1077–1088.

Walpersdorf, A., I. Manighetti, Z. Mousavi, F. Tavakoli, M. Vergnolle, A. Jadidi, D. Hatzfeld, A. Aghamohammadi, A. Bigot, Y. Djamour, H. Nankali, and M. Sedighi (2014), Present-day kinematics and fault slip rates in eastern Iran, derived from 11 years of GPS data, *J. Geophys. Res.*, *119*, 1359–1383.

Wessel, P., and W. H. F. Smith (2013), Generic Mapping Tools: Improved version released, *EOS Trans. Amer. Geophys. U.*, *94*, 409–410.

Zhang, P.-Z. (2013), Beware of slowly slipping faults, *Nature Geoscience*, *6*(5), 323–324.

Zor, E., E. Sandvol, C. Gurbuz, N. Turkelli, D. Seber, and M. Barazangi (2003), The crustal structure of the East Anatolian plateau (Turkey) from receiver functions, *Geophys. Res. Lett.*, *30*(24), 8044.

Table 1. Values of parameters for the best fits to the 367 GPS velocities with homogeneous lithosphere and GPE estimated respectively from topography and from the geoid (Figure 2a,b).

	Ar	$\Gamma_{\rm T}$ TN m^{-1}	$\Gamma_{\rm C}$ TN m^{-1}	$\Gamma_{\rm M}$ TN m^{-1}	B Pa s$^{1/n}$	M (Eq. (12)) mm yr^{-1}	RMS misfit (Eq. (13)) mm yr^{-1}
			GPE from Topography (Figure 3a)				
$n=1$	2.75	-2.25	0.25	-0.6	$1.6\times10^{22\dagger}$	3.3	2.8
$n=3$	6.0	-4.0	0.5	-3.0	3.3×10^{12}	3.4	2.9
$n=5$	9.0	-4.5	-0.5	-3.0	2.9×10^{10}	3.4	3.0
$n=9$	11.5	-5.0	-1.0	-3.0	1.3×10^{9}	3.5	3.2
			GPE from Geoid (Figure 3b)				
$n=1$	4.25	-1.75	-0.75	-0.6	$1.0\times10^{22\dagger}$	2.8	2.4
$n=3$	8.5	-2.75	0.0	-3.0	2.3×10^{12}	2.7	2.4
$n=5$	10.5	-2.75	0.0	-3.0	2.5×10^{10}	2.7	2.3
$n=9$	11.5	-2.5	0.5	-3.0	1.3×10^{9}	2.9	2.4

†For a Newtonian fluid, the viscosity, η, is equal to half the viscosity coefficient, B (Eq. (9)).

Table 2.   Values of parameters for the best fits to the observed velocities with $n{=}3$, GPE calculated from the geoid, and viscosity coefficient in the relevant region (Figure 6) differing by a factor, B', from that in the rest of the calculation domain (TIP: Turkish-Iranian Plateau; CIP: Central Iranian Plateau; ZAG: Zagros. Γ_T and Γ_C are held fixed at, respectively -2.5 and 0 TN m^{-1}. The first three rows correspond to calculations in which B' varies in one region at a time; the fourth row shows the best-fitting parameters when B' varies in all three regions at once. In each case, the misfits are calculated for all 367 GPS velocities.

| Ar | B'_{TIP} | B'_{CIP} | B'_{ZAG} | B_{TIP} | B_{CIP} | B_{ZAG} | M | RMS misfit |
				\multicolumn{3}{c}{10^{12} Pa s$^{1/n}$}	(Eq. (12)) mm yr^{-1}	(Eq. (13)) mm yr^{-1}
8.5	1.1	1	1	2.5	2.3	2.3	2.7	2.4
9.0	1	0.80	1	2.2	1.7	2.2	2.7	2.3
9.0	1	1	0.85	2.2	1.9	2.2	2.6	2.2
7.9	1.2	1.0	0.83	2.9	2.5	2.0	2.6	2.2

Table 3. Notation.

B	Viscosity coefficient	Equation (7)
G	Gravitational constant	6.67×10^{-11} m^3 kg^{-1} s^{-2}
g	Acceleration due to gravity	9.8 m s^{-2}
h	Surface height	Figure 1
h_0	Reference surface height	100 m
L	Thickness of the lithosphere	100 km
N	Geoid height	
S	Crustal thickness	
S_0	Reference crustal thickness	35 km
u_i	i^{th} component of velocity	
U_0	velocity scale	30 mm/yr
$\dot{\varepsilon}_{ij}$	ij^{th} component of strain-rate tensor	
E	Second invariant of strain-rate tensor	Equation (8)
η_{eff}	Effective viscosity	Equation (9)
Γ	Gravitational potential energy	N m^{-1}
	per unit surface area	or J m^{-2}
ρ_c	Density of crust	2800 kg m^{-3}
ρ_m	Density of mantle	3300 kg m^{-3}
τ_{ij}	ij^{th} component of deviatoric stress tensor	
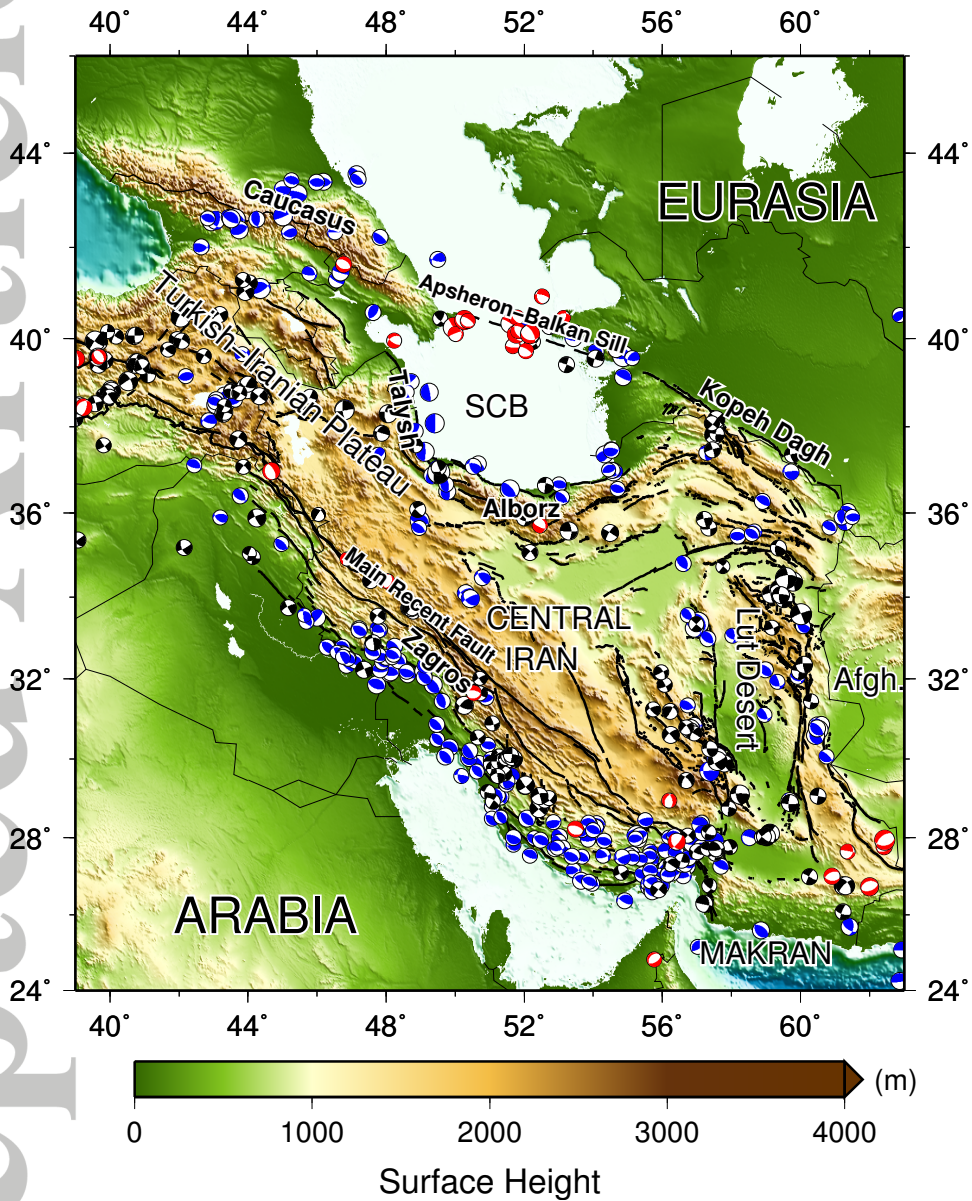
Figure 1. Shaded relief map of Iran showing active faults [*Walker et al.*, 2009], and seismicity from the Global Centroid Moment Tensor Catalog [*Dziewonski et al.*, 1981; *Ekström et al.*, 2012]. Blue, black and red focal mechanisms show thrust, strike-slip and normal faulting events respectively. Labels show locations of places and features referred to in the text. SCB refers to the South Caspian Block
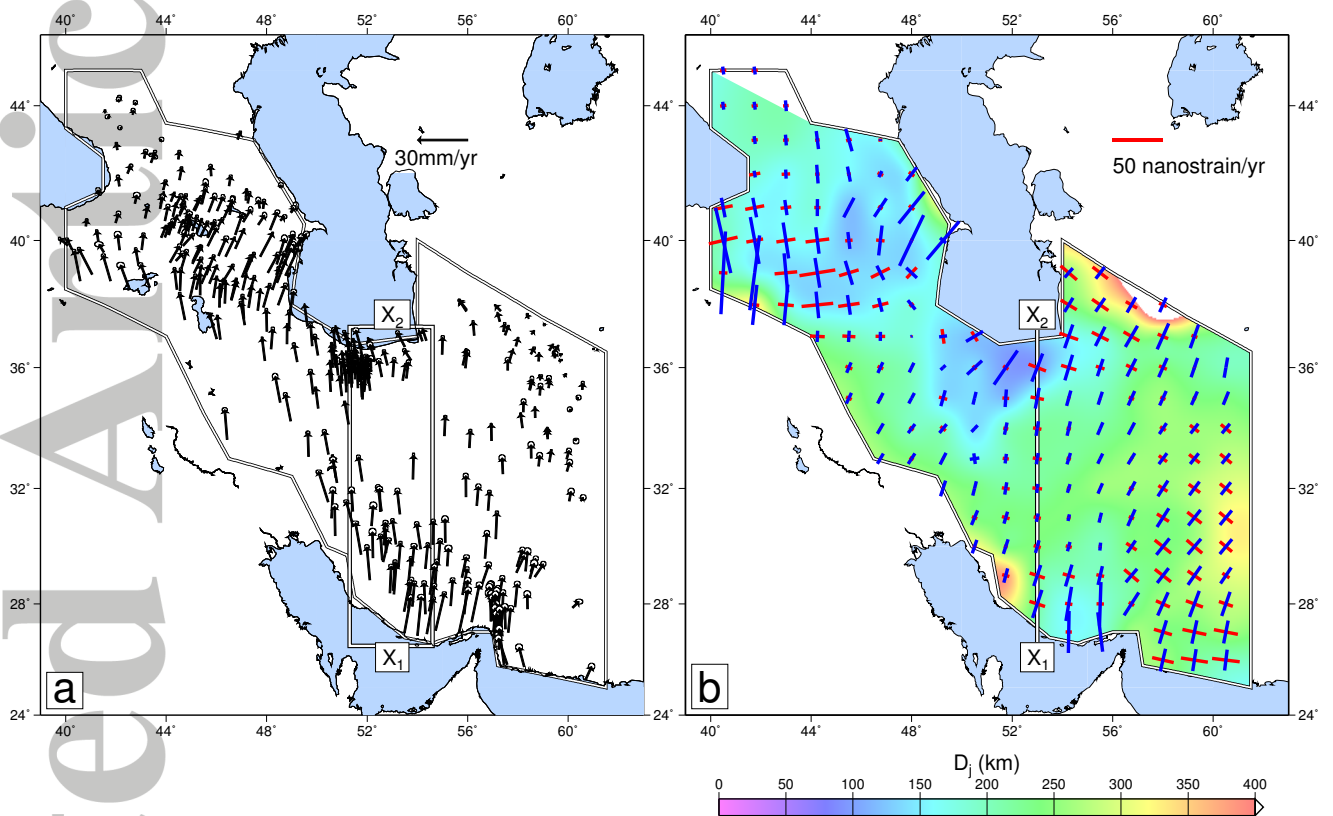
Figure 2. GPS velocities, relative to Eurasia and strain rates derived from them. (a) The subset of GPS measurements [from *Kreemer et al.*, 2014] that is used in this paper (see Section 2.4). The box contains the the sites within 200 km of the profile X₁–X₂ shown in (b), whose velocities are plotted in Figure 4. The polygon shows the boundary of the calculation domain. (b) Orientations and magnitudes of principal axes of strain rate calculated from the velocities shown in (a) using the method of *Shen et al.* [2015] (Section A1). Extensional principal axes are shown by red bars, contraction by blue bars (scale at top right). Background colors (scale at bottom) show the distribution of smoothing distances D_j using a weighting (see Section A1) that gives a median smoothing distance of 160 km. Line X₁–X₂ shows the profile analysed in Section 3 and shown in Figure 4.
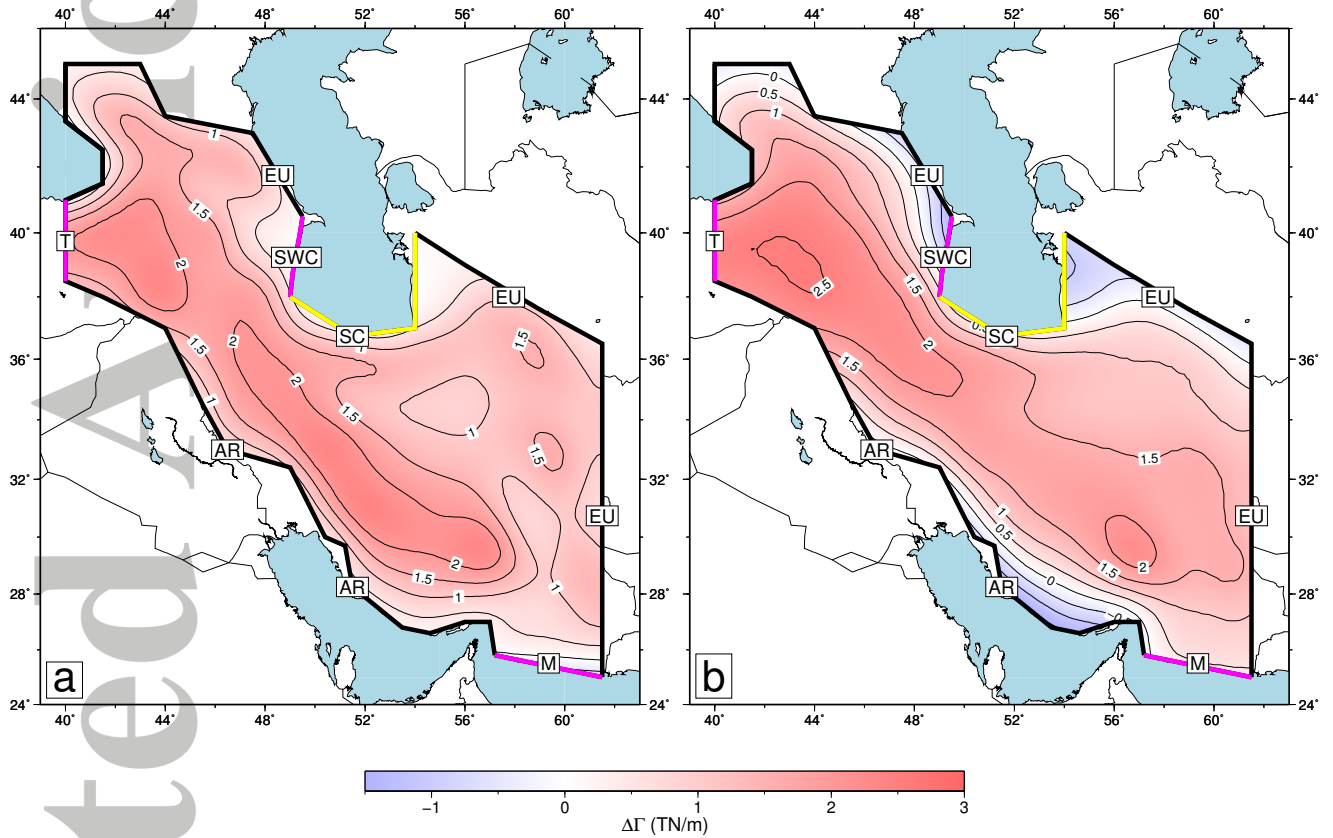
Figure 3.   Boundary conditions and GPE distributions used in calculations. (a) GPE from topography, filtered with a 100-km-diameter Gaussian filter, calculated using Equation 5. (b) GPE calculated from the EGM08 geoid as described in Section 2.1. The edges of the model domain are delineated by the thick lines; black and yellow boundaries have a fixed velocity condition, and magenta boundaries have boundary-normal forces per unit length. The lettered codes refer to individual boundary conditions, see Section 2.3 for descriptions of conditions applied to each boundary.
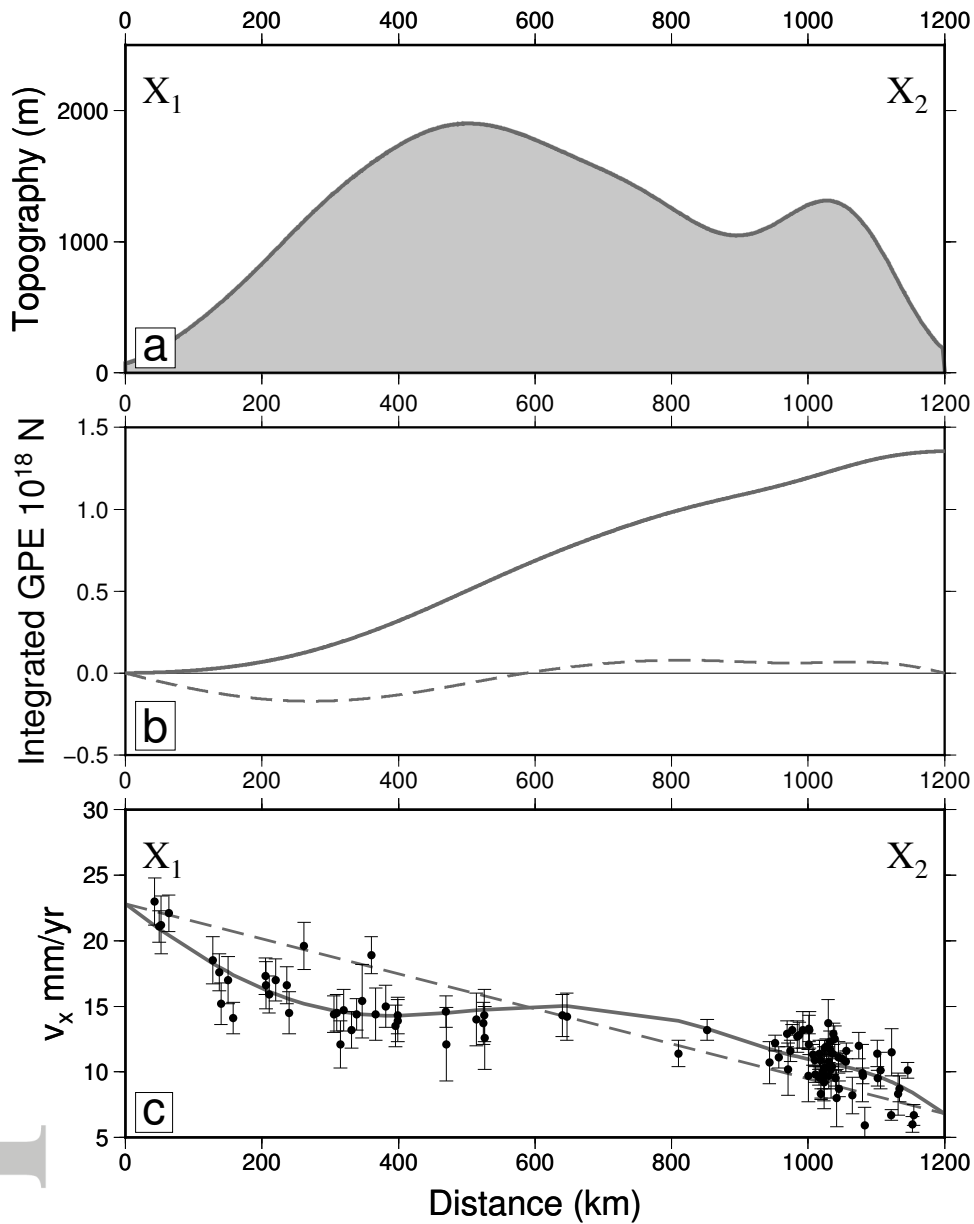
Figure 4. Smoothed surface height, integrated GPE, and velocity along profile X_1–X_2 across central Iran (Fig. 2). (a) Shading shows the topography, averaged over 200 km either side of the profile. (b) Dark grey line shows the integral, from the origin to the relevant distance, of the GPE excess relative to the reference column: $\int_0^x \Delta\Gamma(x')\mathrm{d}x'$, Eq. (11); this quantity is calculated from the topography using Eq. (5). Dashed line shows the term in square brackets in Eq. (11). (c) Circles with error bars show component of velocity parallel to the profile from sites within 200 km of the profile; uncertainties are shown at the 2-σ level. Grey line shows the best fit to observed velocities (Eq. (11)); dashed line shows the linear part of this fit (first two terms in Eq. (11)).
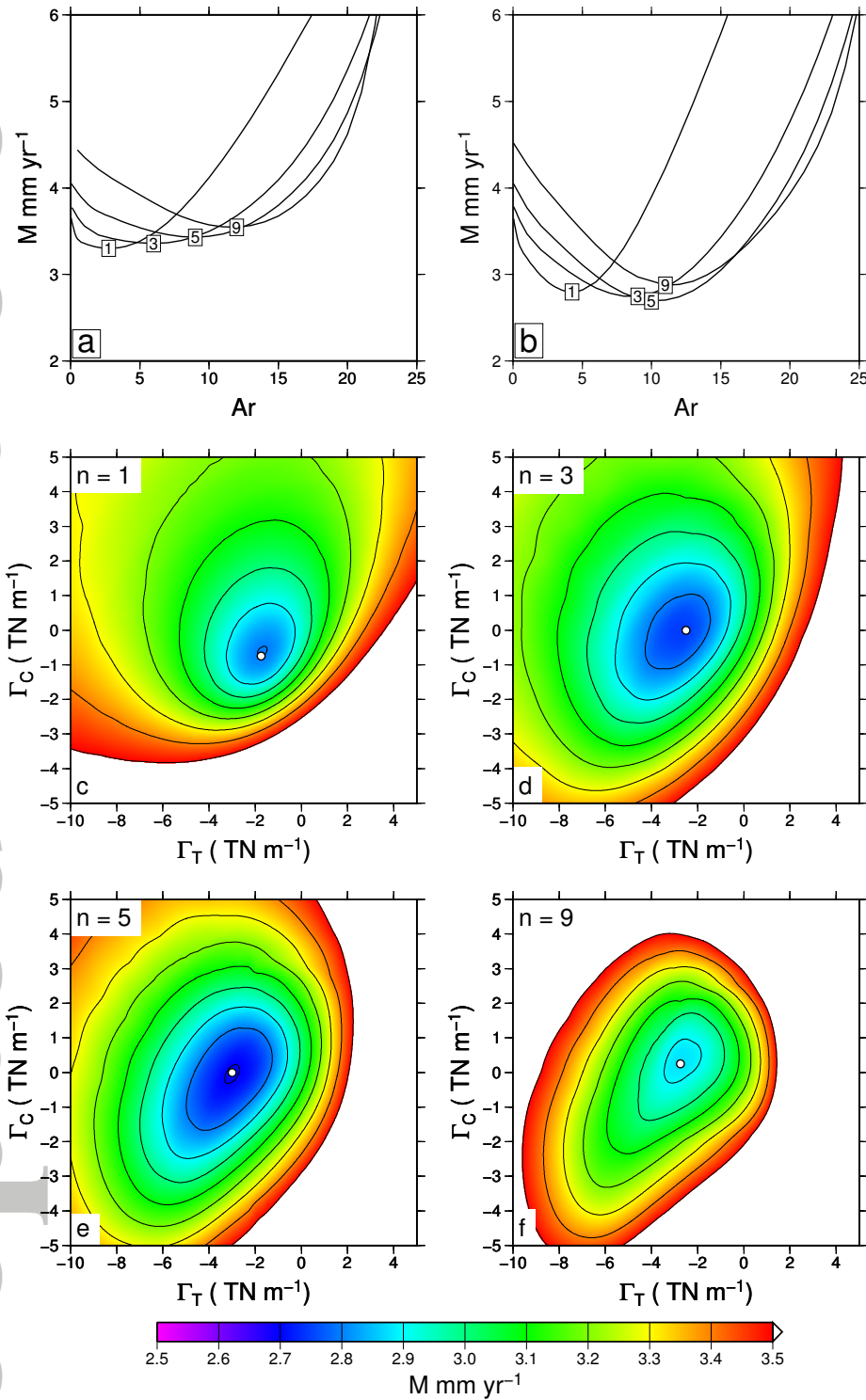
Figure 5. RMS misfits between calculations and GPS velocities (Table 1). (a) Minimum values of M (Eq. (12)) obtained for calculations using GPE derived from an Airy isostatic model of topographic support (Figure 3a), varying the boundary forces Γ_T and Γ_C as described in Section 4.1. Curves show, for each value of n, the value of Ar at which the minimum is found; numbers on each curve are at the minima, and denote the value of n. (b) As for (a), but for calculations with the GPE calculated from the geoid (Figure 3b). (c-f) Distribution of M for calculations using GPE derived from the geoid; colors show the lowest value of M for each combination of Γ_T and Γ_C; white circles correspond to the minima in (b).
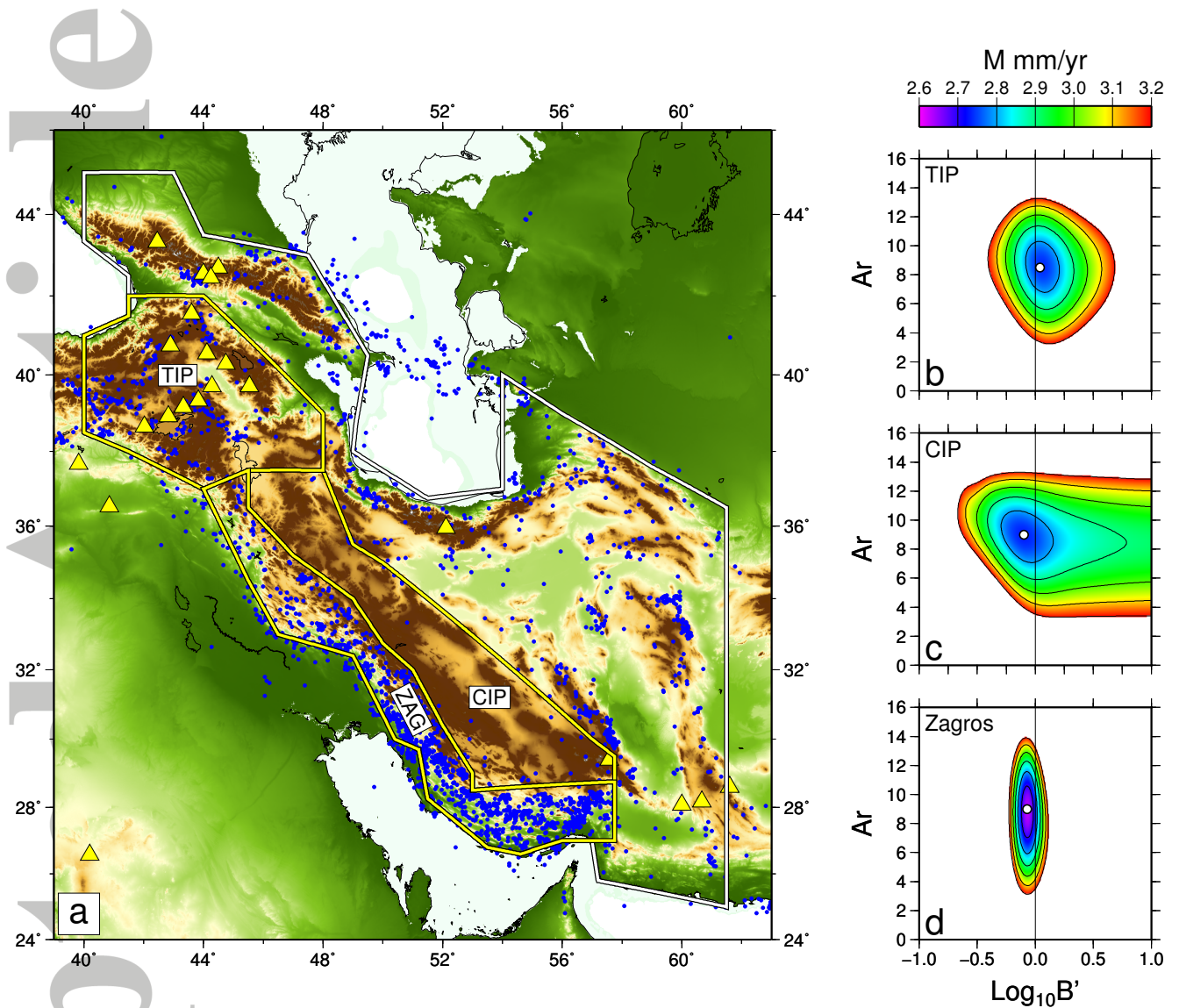
Figure 6. Calculations including lateral heterogeneity in material properties of the lithosphere. (a) Yellow lines outline the Turkish-Iranian Plateau (TIP), Central Iranian Plateau (CIP), and the Zagros Mountains (ZAG); white line encloses region of calculation. Blue dots indicate epicentres of shallow earthquakes in the interval 1964–2010 and yellow triangles show locations of volcanoes active in the Holocene [*Siebert and Simkin*, 2002]. (b) Distribution of weighted misfit, M Eq. (12), for calculations with $n=3$ and GPE calculated from the geoid. B' of Turkish-Iranian Plateau was varied from 0.1 to 10, and Γ_T and Γ_C were fixed to their best-fitting values for the calculations with spatially invariant material properties. Colors show the lowest value of M for each combination of B' and Ar. (c) As for (b), but for cases in which B' was varied for the Central Iranian Plateau. d) As for (b), but for cases in which B' was varied for the Zagros.
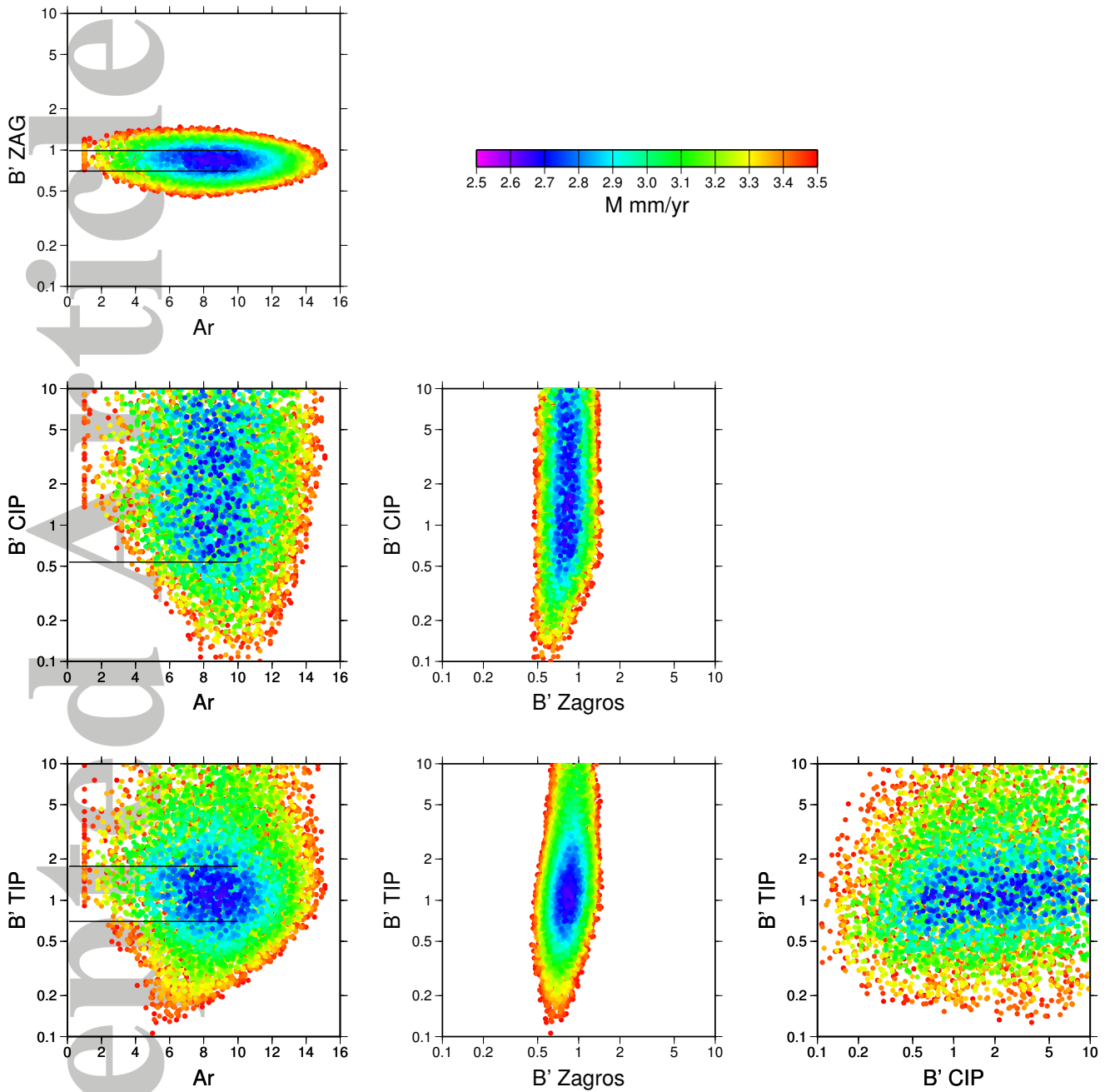
Figure 7. Weighted misfits M (Eq. (12)) for 100,000 random combinations of Ar and B' in the Turkish-Iranian Plateau (B'_{TIP}), Central Iranian Plateau (B'_{CIP}), and Zagros, (B'_{ZAG}). In each panel, colored dots (scale at top) show the minimum value of M obtained in the two-dimensional slice through the four-dimensional parameter space. Horizontal lines in the left-hand column show the ranges of B' for which M is lower than for the best-fitting solution for the homogeneous sheet with $n = 3$.
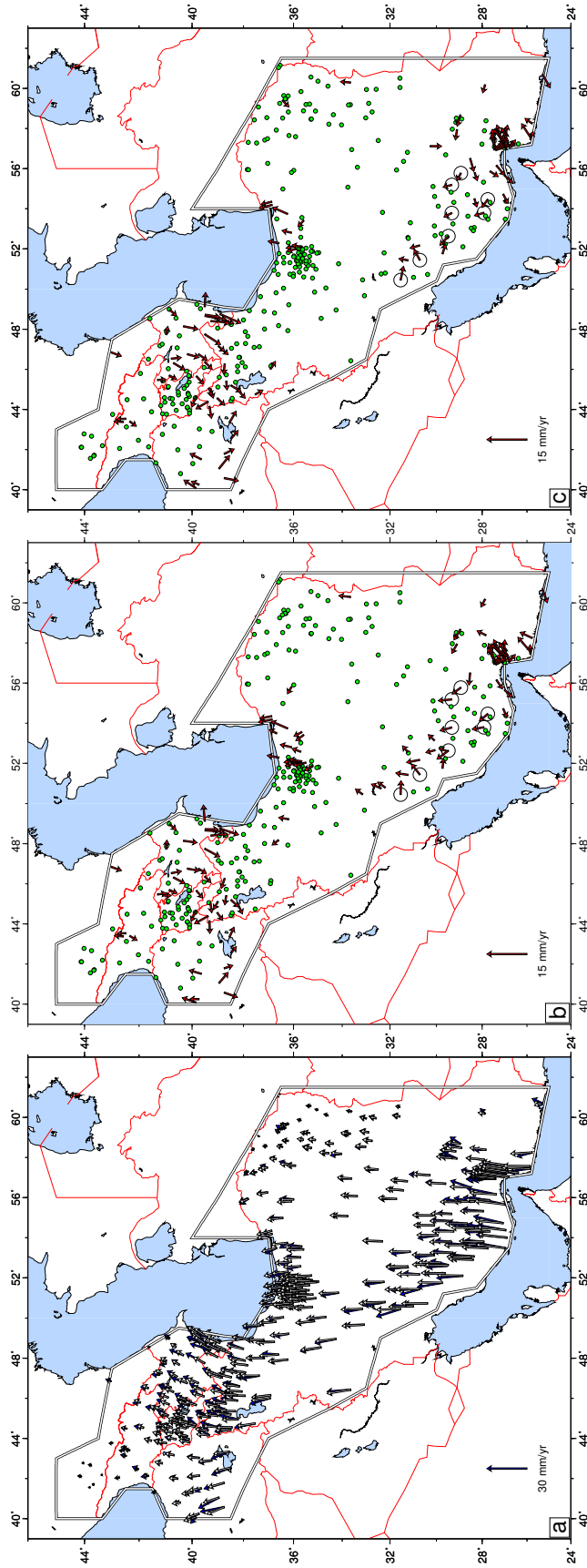
Figure 8. Best-fitting solution for $n = 3$ and GPE calculated from the geoid (Figure 3b). (a) Blue arrows show the observed GPS velocities (Figure 2a) and white arrows show calculated velocities. (b) Red arrows (at twice the scale of the white and blue arrows) show (calculated - observed GPS velocities) for sites with residual velocities of magnitude >3 mm/yr. Green circles are the 264 out of 367 sites for which the residual velocities have magnitudes ≤3 mm/yr. (c) As for (b) for the best-fitting calculation in which the viscosity coefficients of the Zagros and the Central Iranian and Turkish-Iranian plateaux are allowed to vary (Section 4.2).
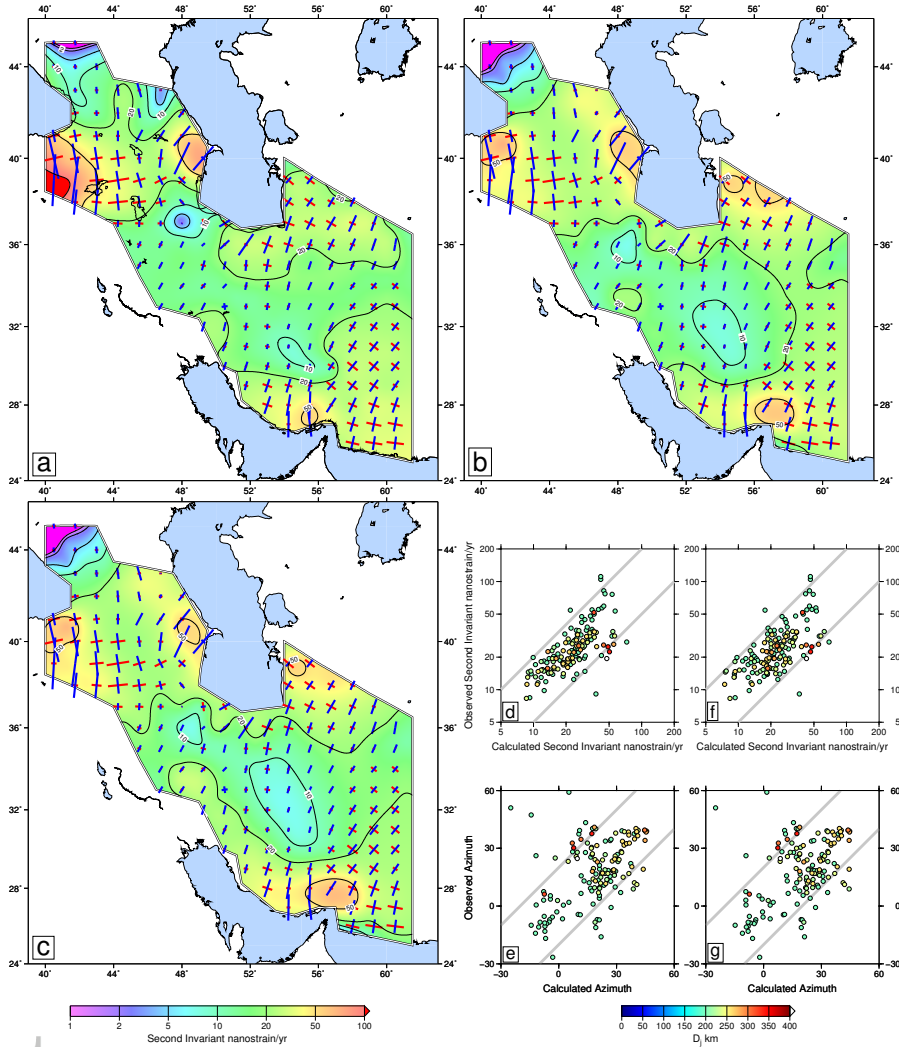
Figure 9. Comparison between observed and calculated strain rates. (a) Distribution of the second invariant of the strain-rate tensor calculated from GPS velocities (Figure 2b and Section A1). Superimposed crosses show the orientations and magnitudes of the principal horizontal axes of strain rate. (b) As for (a), for the best-fitting calculation with laterally invariant material properties (Figure 8a,b). (c) As for (a), for the best-fitting calculation with B' allowed to vary (Figure 8c). (d) Comparison between observed and calculated values of the second invariant of the strain rate tensor (Eq. (8)) at the location of each of the cross symbols in (a) and (b). (e) Comparison between the azimuths of the principal horizontal axis of contraction at the location of each of the cross symbols in (a) and (b). Symbols are colored according to the value of the smoothing distance (D_j, Section A1) at the geographical location of the observation. (f, g) as (d, e) but comparing the strain-rate field of (c) with that of (a).
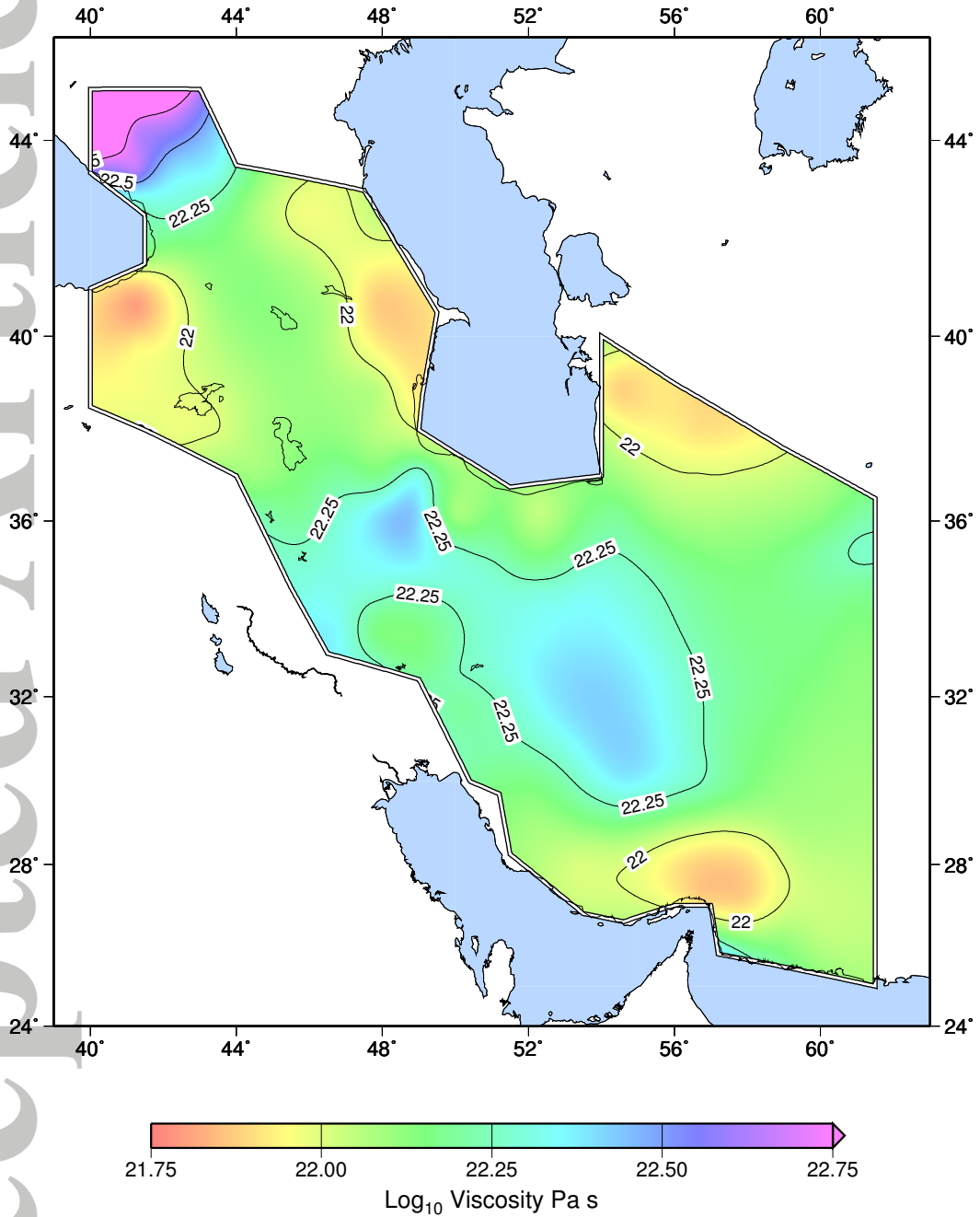
Figure 10. Calculated distribution of effective viscosity (η_{eff}, equation (9)) for the best-fitting calculation with laterally invariant material properties (Figure 8).
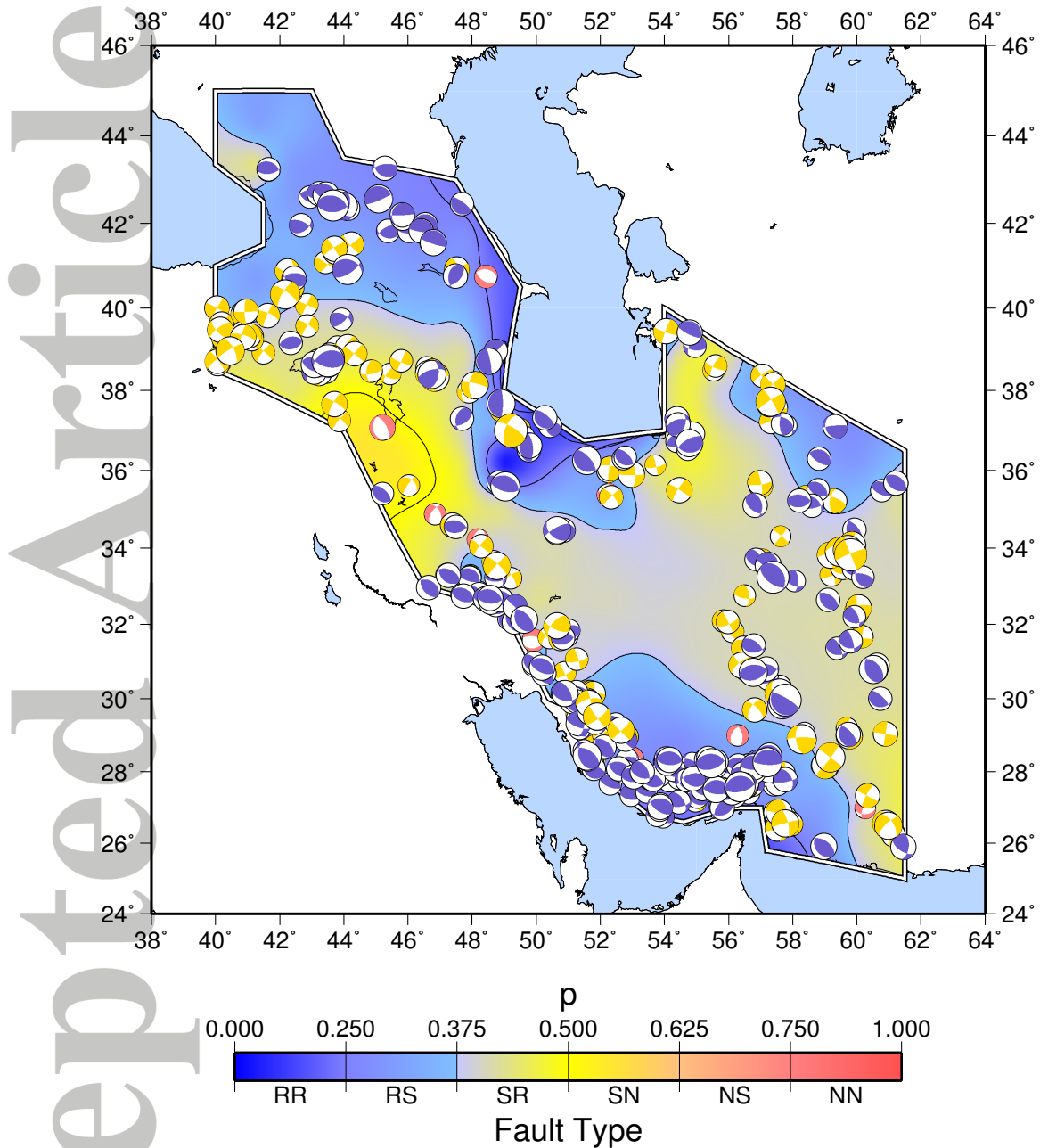
Figure 11.   Predicted distributions of fault types for the best-fitting calculation with laterally invariant material properties and *n*=3 (Figure 8) compared with the observed distribution earthquake focal mechanisms. Colors show the predicted distribution of fault types from the model strain rate field (equation (14), Section 5.2); in the two-letter designations, N, S, R, refer to normal, strike-slip, and reverse faulting with the first letter referring to the type of faulting that accommodates the greater fraction of strain rate. Focal mechanisms are from the GCMT catalogue [*Dziewonski et al.*, 1981; *Ekström et al.*, 2012]; reverse- strike-slip- and normal-faulting earthquakes are shown with blue, gold, and red compressional quadrants, respectively.
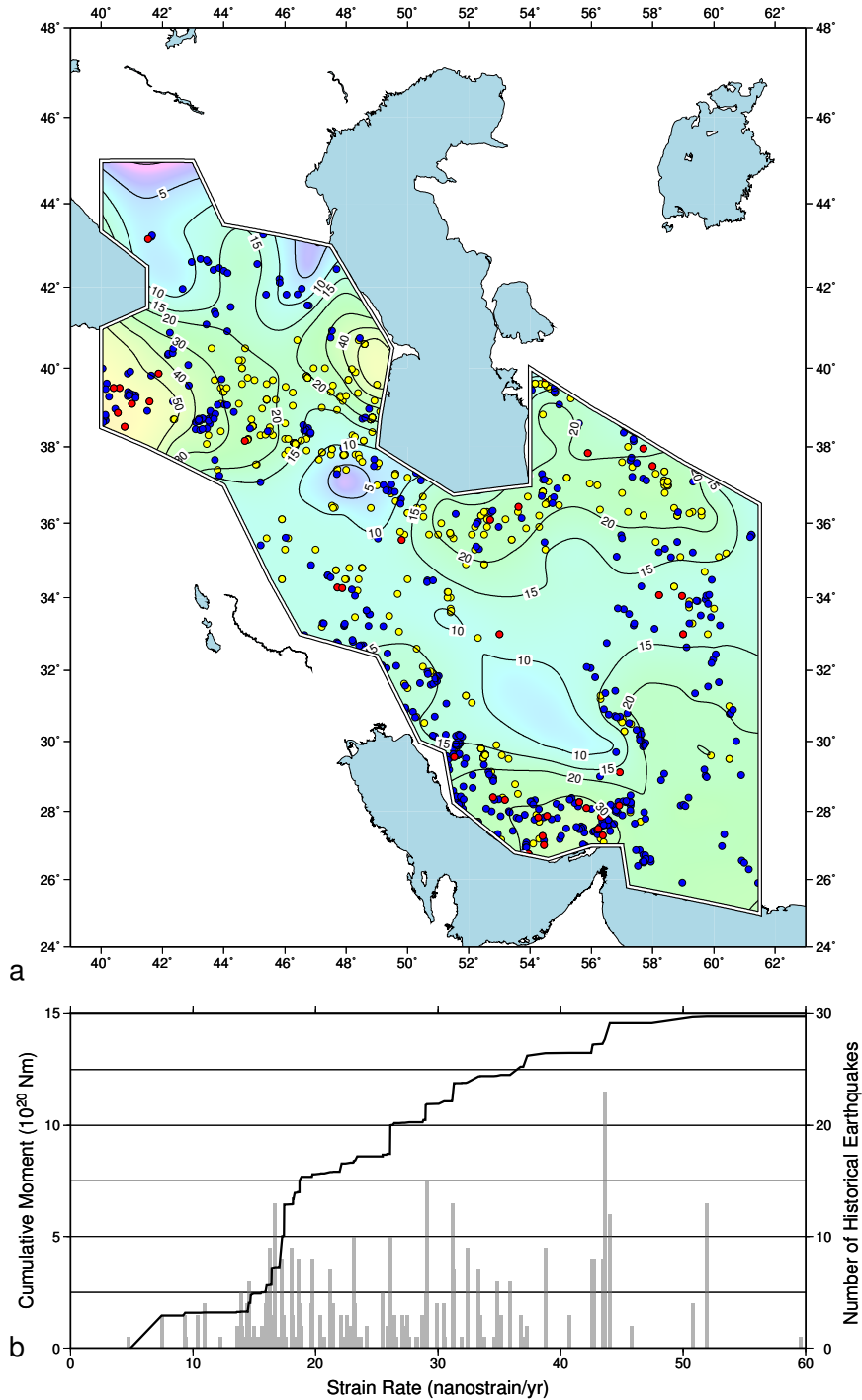
Figure 12. (a) Distribution of the second invariant of the strain-rate tensor calculated from GPS velocities (Figure 9a), in units of nanostrain per year. Blue dots show the epicenters of earthquakes in the GCMT catalog [*Dziewonski et al.*, 1981; *Ekström et al.*, 2012]; red dots show epicenters of earthquakes between 1900 and 1976 [*Engdahl and Villaseñor*, 2002]; yellow dots show the epicenters of earthquakes before 1900 [*Ambraseys and Melville*, 1982]. (b) Black line shows cumulative moment release for the earthquakes in the GCMT catalog allocated to 100×100 km^2 boxes, arranged in order of increasing strain rate of those boxes. Grey vertical lines show the number of earthquakes [*Ambraseys and Melville*, 1982; *Dziewonski et al.*, 1981; *Ekström et al.*, 2012; *Engdahl and Villaseñor*, 2002] that occurred within each box.
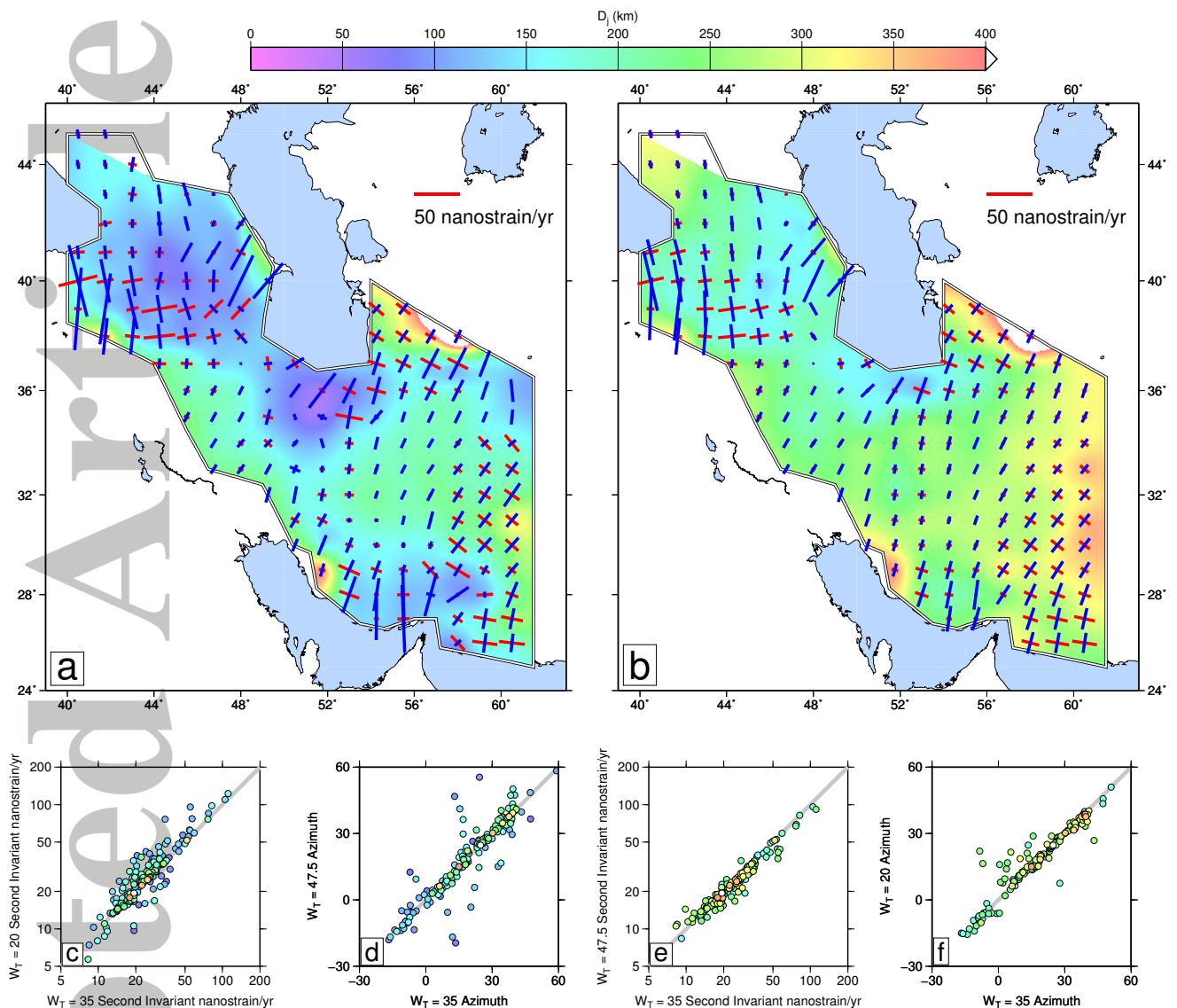
Figure 13. Comparison between strain-rate fields calculated using the method of *Shen et al.* [2015] with different degrees of smoothing. (a) Orientations and magnitudes of principal axes of strain rate calculated from the velocities shown in Figure 2a. Extensional principal axes are shown by red bars, contraction by blue bars. Background colors show the distribution of smoothing distances D_j calculated the velocities using a weight of $W_T=20$, which gives a median smoothing distance of 120 km. (b) As for (a), but with a weight of $W_T=47.5$, which gives a median smoothing distance of 200 km. (c) Comparison between values of the second invariant of the strain rate tensor (Eq. (8)) calculated at the location of each of the cross symbols in (a) with $W_T=20$ and with $W_T=35$, which is the value adopted in the body of the text. (d) Comparison between the azimuths of the principal horizontal axis of contraction calculated with $W_T=20$ and 35. Symbols are colored according to the magnitude of the second invariant of strain rate in (a). (e, f) as for (c, d), but comparing strain-rate fields calculated with $W_T=47.5$ and 35. Symbols are colored according to the magnitude of the second invariant of strain rate in (b).